

RICE UNIVERSITY

**Profiling the Near field of Nanoshells using Surface Enhanced
Raman Spectroscopy and Fluorescence Spectroscopy**

by

Surbhi Lal

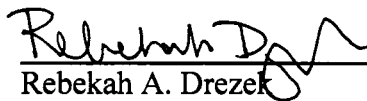
A THESIS SUBMITTED
IN PARTIAL FULFILLMENT OF THE
REQUIREMENTS FOR THE DEGREE

Doctor of Philosophy

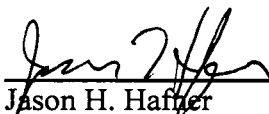
APPROVED THESIS COMMITTEE:



Naomi J. Halas, Chair
Stanley C. Moore Professor in Electrical and
Computer Engineering and
Professor of Chemistry



Rebekah A. Drezek
Stanley C. Moore Assistant Professor of
Bioengineering and Assistant Professor of
Electrical and Computer Engineering



Jason H. Hafner
Assistant Professor of Physics and Astronomy
and Assistant Professor of Chemistry

HOUSTON, TEXAS
May 2006

UMI Number: 3216736

INFORMATION TO USERS

The quality of this reproduction is dependent upon the quality of the copy submitted. Broken or indistinct print, colored or poor quality illustrations and photographs, print bleed-through, substandard margins, and improper alignment can adversely affect reproduction.

In the unlikely event that the author did not send a complete manuscript and there are missing pages, these will be noted. Also, if unauthorized copyright material had to be removed, a note will indicate the deletion.



UMI Microform 3216736

Copyright 2006 by ProQuest Information and Learning Company.

All rights reserved. This microform edition is protected against unauthorized copying under Title 17, United States Code.

ProQuest Information and Learning Company
300 North Zeeb Road
P.O. Box 1346
Ann Arbor, MI 48106-1346

Abstract

Profiling the Near Field of Nanoshells Using Surface Enhanced Raman Spectroscopy and Fluorescence Spectroscopy

By

Surbhi Lal

Plasmon resonances in metal nanoparticles control the far field and near field optical properties of these metallic structures. The enhanced electromagnetic near field is strongest at the surface of the nanoparticles and rapidly decays away from the surface. This enhanced near field is exploited in surface enhanced spectroscopies including Surface Enhanced Raman Spectroscopy (SERS) and Metal Enhanced Fluorescence Spectroscopy (MEFS). A measurement of the decay profile of the fringing field is important both for further development of surface enhanced spectroscopy for sensor device application, and for understanding from a fundamental physics point of view.

Gold nanoshells are spherical colloidal nanoparticles with a silica core covered by a thin gold shell. The plasmon resonance of nanoshells can be controllably tuned in the visible and infrared parts of the spectrum. The near field profile of nanoshells can be theoretically calculated on the basis of Mie scattering theory.

The thesis describes a series of experiments designed to experimentally verify the near field profile of nanoshells. A scaffold of ss-DNA is used to place a fluorescein dye molecule at varying distances from the nanoshell surface. The SERS intensity from both the scaffold molecules and the fluorescein placed at the end of the tether is measured

simultaneously and self consistently. The fluorescein-ss-DNA nanoshell conjugate structures are also used to study the distance dependence of the fluorescence emission from fluorescein. The thesis discusses the results of the SERS intensity profile agreement with the intensity profile calculated using Mie scattering theory. The quenching and enhancement of the fluorescence emission at varying distances from the nanoshell surface are also discussed.

Acknowledgements

.....What a long strange trip its been.

I'm sure The Grateful Dead were not talking about Grad School when they sang that but it does sum up my life in grad school.

The past six years of my life have been the six of the most amazing and enjoyable years of my life. The freedom to pursue research in so many different directions, to also watch everyone grow as scientists and accomplish great results with their research has been a joy and intellectually very stimulating. I have a lot of people to acknowledge for contributing to my sense of fulfillment.

I would like to first thank Dr. Naomi Halas for providing an atmosphere, which always encouraged creativity and excellence. Most of all she encouraged me to try projects in such a variety of fields that I am a better physicist and yet I am more than a physicist because of it. On a more personal level I am truly grateful for her support when I took an extended maternity leave. Her positive attitude in helping women scientists deal with family issues has helped at least one woman scientist achieve her dreams of doing science.

I owe an equally big THANK YOU to all the members of the Halas group for stimulating interactions. I have learned from all of you. Thanks to Nate and Joe for nanoshell code help and coffee when I needed both the most. A special thanks to Glenn who taught me all the DNA chemistry I know. Greg, Sarah and then Corey, Cristin who were there to answer all my questions. A thank you to Lee who made all the biochemistry seem easy. I have truly benefited from all the exchanges with other group members:

Carly, SriPriya, Nikolay, Sandra, Jennifer, Bruce, Joe Cole, Hui, Yu, Felicia, Britt, Jeremy, Janardhan, Zaw and Donald. If I've missed out anyone its due to a lack of caffeine.

Outside the group I would like to thank Dr. Peter Nordlander for help with the theory of plasmon - plasmon interactions. I have looked forward to and learned a lot from the impromptu tutorials you gave at the LANP meetings. Thanks are due to Dr. Rebekah Drezek for allowing me unlimited use of the fluorometer. I will not easily forget the many hours spent in front of that machine.

The network of people who have contributed to my success extends far beyond the hedges at Rice. I am ever grateful for the love and support of my parents and family who always believed I would be a good scientist. I am grateful to my father-in-law who always encouraged me to continue work on my Ph.D.

Finally I wish to express my deepest love and gratitude to Sandeep my husband, and Anant and Udit my sons, who have shared all the highs and lows of research and grad school. None of this would have been possible without your love, support, inspiration, and sacrifices.

Table of Contents

Abstract	i
Acknowledgements.....	iii
Table of Contents	v
Table of Figures	vii
Table of Tables	x
Chapter 1 : Introduction.....	1
1.1 Silica-Gold Nanoshells	3
1.2 Surface Enhanced Raman Spectroscopy.....	4
1.3 Metal Enhanced Fluorescence Spectroscopy	5
Chapter 2 : Nanoshell Theory.....	9
2.1 Introduction.....	9
2.2 Plasmon Hybridization	9
2.3 Theoretical Basics of Light Scattering by Nanoshells	11
2.4 Series Expansion of Incident Plane Wave	13
2.5 Series Expansion for the Nanoshell	13
2.6 Nanoshell Far Field Scattering Properties.....	15
2.7 Nanoshell Near Field Scattering	16
2.8 Homogeneous and Inhomogeneous Broadening	16
2.9 SERS Enhancement Calculation	18
Chapter 3 : Experimental Considerations and Sample Preparation.....	20
3.1 Introduction.....	20
3.2 Silica Gold Nanoshell fabrication	20

3.3	<i>Nanoshells for SERS Experiments</i>	22
3.4	<i>Nanoshells for Fluorescence Measurements</i>	24
3.5	<i>ss-DNA as Tether for Building a Nano-scaffold</i>	26
3.6	<i>ss-DNA Sequences used for the SERS and Fluorescence Measurements</i>	29
3.7	<i>Cleaving and Desalting the ss-DNA</i>	30
3.8	<i>Preparation of Nanoshell-ss-DNA conjugates for SERS experiments</i>	30
3.9	<i>Nanoshell ss-DNA conjugates for fluorescence measurements</i>	33
3.10	<i>Mixed ss-DNA and Mercaptohexanol layers on Nanoshells</i>	34
3.11	<i>Quantifying the surface coverage of ss-DNA on Nanoshells</i>	35
3.12	<i>Conclusion</i>	36
Chapter 4 :	SERS and Fluorescence Results	37
4.1	<i>Introduction</i>	37
4.2	<i>Surface Enhanced Raman Scattering from ss-DNA-Nanoshell Conjugates</i>	38
4.3	<i>Fluorescence Results</i>	45
4.4	<i>Fluorescein, Nanoshells and pH</i>	49
4.5	<i>Conclusion</i>	51
Chapter 5 :	Light Interaction between Nanoshell Plasmons and Planar Waveguides	52
5.1	<i>Introduction</i>	52
5.2	<i>Experimental Techniques</i>	53
5.3	<i>Results and Discussion</i>	55
5.4	<i>Conclusion</i>	63
Chapter 6 :	Conclusions	66
Bibliography	70

Table of Figures

Figure 1.1: Raman scattering process	4
Figure 1.2: Jablonski diagram for the fluorescence processes in free space and close to a metal surface.	7
Figure 2.1 Plasmon Hybridization for Gold Nanoshells.....	10
Figure 2.2 : Schematic of a Nanoshell Showing the various parameters.....	14
Figure 3.1 : Far field spectrum (black) and the calculated surface average near field spectrum (red) for $[r_1, r_2] = [70, 91]$ nm nanoshells. The excitation laser at 785 nm (red line), the emission peak wavelengths for the adenine (blue) and fluorescein (green) are included. The spectra are scaled for clarity.	23
Figure 3.2 : Extinction spectrum (black) and the calculated surface average near field spectrum (red) for $[r_1, r_2] = [43, 58]$ nm nanoshells. The excitation laser at 785nm (red line), the stokes emission peak wavelengths for the adenine (blue) and fluorescein (green) are included. The spectra are normalized for clarity.	24
Figure 3.3 : Absorbance spectrum of nanoshells used for fluorescence measurements. The absorption and emission maximum wavelengths for fluorescein are included.	25
Figure 3.4 : a) Schematic illustrating the different lengths of the ss-DNA nano-scaffold used to place the fluorescein at different places in the near field of the nanoshell. b) Schematic of the thiolated ss-DNA-fluorescein conjugate structure with 2 adenine bases.....	26
Figure 3.5 : Absorption and emission spectra of fluorescein at pH 8.5.....	27
Figure 3.6: (Top)Dark field image of nanoshell-DNA conjugates immobilized on quartz slides. (Bottom) SEM images of nanoshell-DNA conjugates immobilized on quartz	

slides(left) $[r_1, r_2] = [70, 91]$ nm shells and (right) for $[r_1, r_2] = [43, 58]$ nm nanoshells	32
Figure 3.7: Schematic illustrating the steps involved in fabricating nanoshell-DNA-MCH conjugate structures for fluorescence measurements.....	33
Figure 4.1 : Schematic representation of the adenine-fluorescein conjugate structure attached to a nanoshell (not to scale). The adenine and fluorescein moieties are accurately depicted in Figure 3.4	39
Figure 4.2: SERS spectra for the 4 lengths of adenine strands (left) nanoshell extinction tuned to the excitation laser (70-91 nm) and (right) nanoshell near field tuned to the pump laser (40-58 nm). The number of adenine moieties in the scaffold molecules is indicated on the left of each spectrum.	40
Figure 4.3: SERS spectra of adenine strands (without fluorescein) on the $[r_1, r_2] = [70, 91]$ nm size nanoshells. Number of adenine moieties per molecule in the scaffold molecules is indicated on the left of each spectrum.....	40
Figure 4.4: Intensity of the 1185cm^{-1} peak due to fluorescein (left) for $[r_1, r_2] = [70, 91]$ nm shells (squares) and (right) for $[r_1, r_2] = [43, 58]$ nm nanoshells (circles).	42
Figure 4.5: Intensity of the 736cm^{-1} peak due to adenine (left) $[r_1, r_2] = [70, 91]$ nm shells (squares) and (right) for $[r_1, r_2] = [43, 58]$ nm nanoshells (circles).	42
Figure 4.6 : Relative intensity of Fluorescein to adenine (left) for $[r_1, r_2] = [70, 91]$ nm shells and (right) for $[r_1, r_2] = [43, 58]$ nm nanoshells.....	43
Figure 4.8 : Packing densities of the different lengths of ss-DNA. The number of bases in each length is denoted next to the data point.	46

Figure 4.9 : Fluorescence per fluorescein molecule attached to nanoshells at different distances from the nanoshell surface.	47
Figure 4.10: Enhancement in fluorescence intensity of fluorescein at different distances from the nanoshell surface b) Near field intensity distribution at 494 nm.	48
Figure 4.11 : pH dependence of the absorption and emission of fluorescein ⁵⁸	49
Figure 5.1 : UV-Visible spectrum (dashed line) and the calculated cross section (solid line) for an aqueous solution of gold nanoshells	53
Figure 5.2 : (a) Schematic diagram of sample geometry. (b) SEM micrograph showing a typical distribution of nanoshells on the dielectric surface.(c) Digital camera photograph of scattered light from samples of thickness varying from 3.4 nm to 85 nm.	55
Figure 5.3: Light scattering spectra for various thickness of spacer layer. The dashed lines are the experimental data and the solid lines are the calculated theoretical spectra.	57
Figure .5.4: Schematic cartoon of the entire energy transfer interaction between the nanoshells and the waveguide structure.....	58
Figure 5.5: Comparison of the experimental light scattering spectra and the shifted theoretical curves. The dashed lines are the experimental data and the solid lines are the calculated theoretical spectra, shifted by amount shown in Table 5.1.....	60

Table of Tables

Table 3.1: List of DNA sequences used for the SERS and fluorescence experiments.	29
Table 5.1: Experimental and theoretical shift in dipole peak position for different spacer layer thickness.....	61

Chapter 1 : Introduction

Metal surfaces or structures such as metal gratings, smooth metal films, metal island films or colloids are known to greatly modify fundamental photo-physical processes such as Raman scattering, fluorescence and absorption¹. Plasmon resonances, which are the collective oscillations of the conduction electrons supported by these metallic structures, as well as the modification in the photonic local density of states, are responsible for many of the unique optical properties of these structures²⁻⁴. The plasmon resonances control the far field and near field optical properties of metallic structures. The enhanced near field is strongest at the surface of the nanoparticles and decays rapidly away from the surface⁵. This enhanced near field is exploited in surface enhanced spectroscopies including Surface Enhanced Raman Spectroscopy (SERS)⁶⁻¹⁶ and Metal Enhanced Fluorescence Spectroscopy (MEFS)^{12, 17-20}. The large enhancement factors observed in SERS for molecules in close proximity to the surface have been attributed to enhanced electromagnetic near fields.

A direct measurement of the distance dependence of the near field is important both for further development of surface enhanced spectroscopy for sensor device application, for detection of larger organic molecules like proteins or DNA, and for an understanding from a fundamental physics point of view. For SERS, the response depends on the enhanced field as approximately $\sim |E|^4$. Thus placing the analyte molecule close to the surface elicits the largest SERS signal. On the other hand, metal enhanced fluorescence results from three directly competing phenomenon, the increased excitation rate due to the interaction with the enhanced near field, the quenching rate due to non-

radiative decay mediated by the proximal metal surface, and an increase in the spontaneous emission due to a modification in the local photon density of states relative to free space. Quenching is the dominant process very close to the surface (few nanometers from the surface), whereas metal enhanced fluorescence persists for tens of nanometers²¹. Thus there is an optimal distance from the surface where the fluorescence enhancement is maximal.

The decay profile of the electromagnetic near field for small metal nanoparticles is well known theoretically. It can be calculated using analytical techniques such as Mie scattering theory²². Only recently a few experimental measurements of this near field decay profile have been made. Previous studies have tried monitoring surface plasmon resonance shifts associated with either changing the local dielectric environment around silver colloid coated with a silica layer of varying thickness²³, or monitoring the shifts in plasmon resonances associated with changing the interaction distance between two colloid particles^{24, 25} as a measure of the distance dependence of the near field. Metal enhanced fluorescence studies have also measured the enhancement in signal due to the metal surface, and the quenching of the fluorescence very close to the metal surface^{12, 17-19, 26-28}. The decay of the fringing field away from a smooth continuous metal film using surface enhanced Raman scattering and fluorescence has also been measured¹². While the measurements made on the smooth metal film attempt to correlate the experimental measurements with a theoretically modeled field decay profile, most of the other measurements are in qualitative agreement with an expected decay profile without a detailed theoretical model of the decay profile.

In this thesis, experiments with a special class of metal nanoparticles are presented. Metal nanoshells are small spherical nanoparticles consisting of a silica core and a thin metallic shell. The plasmon resonance of these nanoshells can be varied controllably by varying the dimensions of the core and the thickness of the shell²⁹⁻³¹. The near field profile of nanoshells is calculated theoretically using Mie scattering theory and correlated with the experimentally measured SERS response at varying distances from the nanoshell surface. The distance dependent fluorescence intensity of a fluorophore tethered at varying distances from the nanoshell surface also demonstrates the quenching regime and the fluorescence enhancement regime around a nanoshell.

1.1 Silica-Gold Nanoshells

Metal nanoshells are spherical metallodielectric colloidal particles with a dielectric core and a metallic shell. The plasmon resonance of these particles can be controllably tuned in the visible to infrared part of the spectrum by changing the size of the dielectric core and the thickness of the metal shell. Surface conjugation of Raman active molecules, organic fluorophores, and other molecules of interest can be easily accomplished by established conjugation chemistry techniques. Commonly the strong gold thiol affinity is exploited to tether the molecules of interest to the metal surface. Thus nanoshells make efficient substrates for metal enhanced spectroscopy^{6, 8, 14}. The nanoshells used in the present sets of experiments consist of a silica core covered by a gold shell dispersed in water or an aqueous buffer. The optical properties of these nanoshells can be completely explained on the basis of the Plasmon Hybridization (PH) theory³²⁻³⁶ and Mie scattering theory^{4, 22, 37}. These are elaborated upon in later chapters.

1.2 Surface Enhanced Raman Spectroscopy

Raman scattering is the inelastic scattering of a photon due to its interaction with the vibrational levels of a molecule. The scattered photons may have greater or lesser energy than the incident photons. If the emitted photon has lesser energy than the incident photon the process is known as Stokes emission. On the other hand, if the emitted photon has greater energy than the incident photon the process is known as anti-Stokes emission.

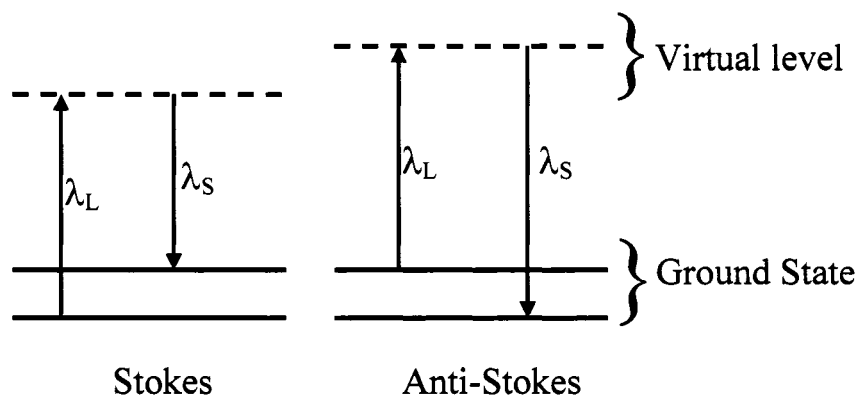


Figure 1.1: Raman scattering process

The intensity of Raman scattered photons depends upon the molecular polarizability of the molecule and thus it is very weak for a large number of molecules. When the molecules are placed in the intense near field associated with metallic nanoparticles, the induced dipole polarizability of the molecules increases. This leads to an increase in the intensity of Raman scattered photons by several orders of magnitude. This enhancement of the Raman scattering is known as Surface Enhanced Raman scattering (SERS).

The enhancement in SERS intensity is due to an enhancement of absorption by the molecule and emission of Raman scattered light. Both enhancement factors are proportional to $|\mathbf{E}|^2$, thus the SERS intensity is enhanced by a factor $\sim |\mathbf{E}|^4$. Another smaller contributing factor to the SERS enhancement is the chemical effect. When a molecule is adsorbed on the metal surface or is bound to the surface it forms a charge transfer state between the adsorbate molecule and the metal surface. This again leads to an increase in the intensity of the Raman scattered light.

SERS is sensitively dependent on the distance between the metal surface and the Raman active molecule because the SERS intensity depends upon the fourth power of the electric field; even small variations in the electric field are magnified in the SERS response. The largest SERS response is expected from molecules directly adsorbed on or attached to the metal surface and a smaller response from molecules tethered away from the surface. As the near field decays, there is a monotonic decrease in the SERS signal.

1.3 Metal Enhanced Fluorescence Spectroscopy

Fluorescence is the emission of light from a singlet-excited electronic state to the ground state of any material. In free space the material absorbs a photon to excite an electron to an excited state. This electron can then relax to the first excited singlet state (S_1). The electron can then return to the ground state by emitting a photon at a rate Γ , or by a non-radiative decay process with a rate k_{nr} . The photophysics of this process is illustrated in the Jablonski diagram in figure 1.2 adapted from Lakowicz³⁸. In the vicinity of a metal surface, the enhanced near field of the metal enhances the absorption rate by E_m . This leads to an overall enhancement in the fluorescence emission. Enhancement factors upto a 100 have been reported. The vicinal metal also provides additional

pathways for non-radiative decay and quenches the radiative decay from the excited state. Thus the quantum yield, defined as the number of emitted photons relative to the number of incident photons, is modified. In free space conditions, the quantum yield is given by

$$Q_0 = \frac{\Gamma}{\Gamma + k_{nr}}. \quad (1.1)$$

and the lifetime which is determined by the sum of all the process that depopulate the excited state is given by

$$\tau_0 = (\Gamma + k_{nr})^{-1} \quad (1.2)$$

In the vicinity of the metal surface the quantum yield is modified to

$$Q = \frac{\Gamma + \Gamma_m}{\Gamma + \Gamma_m + k_{nr}}. \quad (1.3)$$

and the lifetime in the presence of a vicinal metal is modified to

$$\tau = (\Gamma + \Gamma_m + k_{nr})^{-1} \quad (1.4)$$

The optimal distance to place a fluorophore is determined by consideration of the distance scales associated with the quenching due to the presence of the metal surface and the near field enhancement. The quenching effect decays as $\sim d^{-3}$, where d is the distance between the metal surface and the fluorophore. Thus quenching is the dominant effect when the fluorophores are positioned within approximately 5nm of the metal surface. The enhanced near field persists for tens of nanometers and thus enhances the absorption and the radiative decay rate. This implies that there is an optimal distance $d > 5$ nm where the fluorophore is the brightest^{18, 19}.

The third mechanism for the modification of the fluorescence from a fluorophore placed close to a metallic surface is the increase in the radiative emission rate Γ_m . This is due to the modification of the local photon density of states. The quantum yield increases

(Equation 1.3) and the lifetime decreases (Equation 1.4) as the radiative emission rate increases.

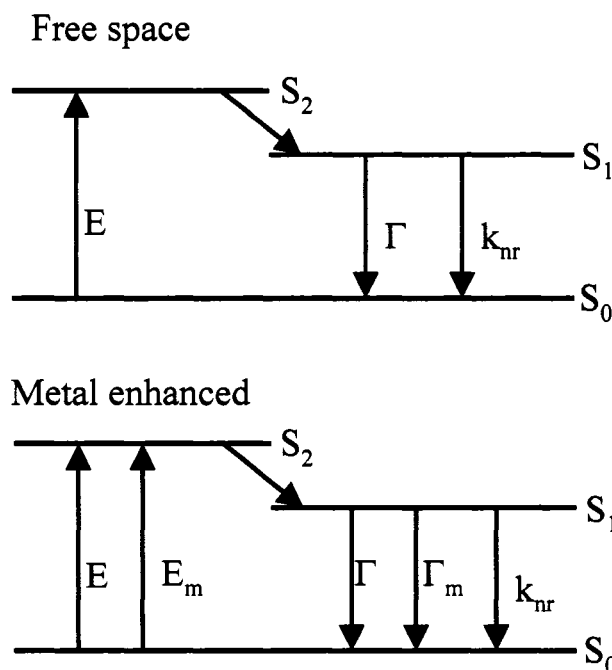


Figure 1.2: Jablonski diagram for the fluorescence processes in free space and close to a metal surface.

This thesis is structured as follows: Chapter 2 outlines the vector basis formalism of Mie scattering theory that is used throughout this thesis to calculate the far field and near field response of the nanoshells and the field decay profiles away from the nanoshells. In Chapter 3 the experimental considerations in designing nanoshells for various experiments are discussed. The various sample geometries and preparations for the SERS and fluorescence measurements are also discussed. Chapter 4 outlines the various SERS and Fluorescence measurements and includes discussion of the results of both sets of experiments. Chapter 5 describes the experimental and theoretical aspects of

the distance dependent interaction of gold nanoshells on a waveguiding structure. Light scattering experiments performed on gold nanoshells randomly deposited on a gold layer with a dielectric spacer layer show a change in the scattering spectrum of the nanoshells due to coupling of light with the waveguide modes in the dielectric layer. Chapter 6 summarizes the results and discusses possible future directions.

Chapter 2 : Nanoshell Theory

2.1 Introduction

The optical properties of metal nanoshells are dominated by the surface plasmon resonance, a collective oscillation of the conduction electrons of the metal shell. There are two approaches to understanding the nanoshell plasmon properties. The near field and far field properties of nanoshells can be intuitively understood on the basis of the plasmon hybridization theory³²⁻³⁶. Alternately, analytical solutions of the electromagnetic problem of a plane wave interacting with a spherical particle are also well known^{4, 22, 37, 39}. This chapter outlines the basic plasmon hybridization theory for nanoshells, and then elaborates on the analytical solution based on Mie scattering theory. This analytical solution of the nanoshell interacting with light is then used to determine the near field and far field properties of nanoshells. The near field decay profile is calculated theoretically based on the same analytical solution of the problem. The distance dependent Raman response for a molecule tethered at varying distances from the nanoshell surface as well as the Raman response of the tether molecules is also calculated using the vector basis formalism.

2.2 Plasmon Hybridization

The surface plasmon resonance wavelength of a nanoshell is determined by the ratio of the core radius to the total particle radius, and the dielectric functions of the core, shell and embedding medium. This allows for a geometric tunability of the plasmon

across the visible and infrared parts of the spectrum by varying the ratio of the core radius to total particle radius. The tunability of the nanoshell plasmon can be explained on the basis of the plasmon hybridization model.

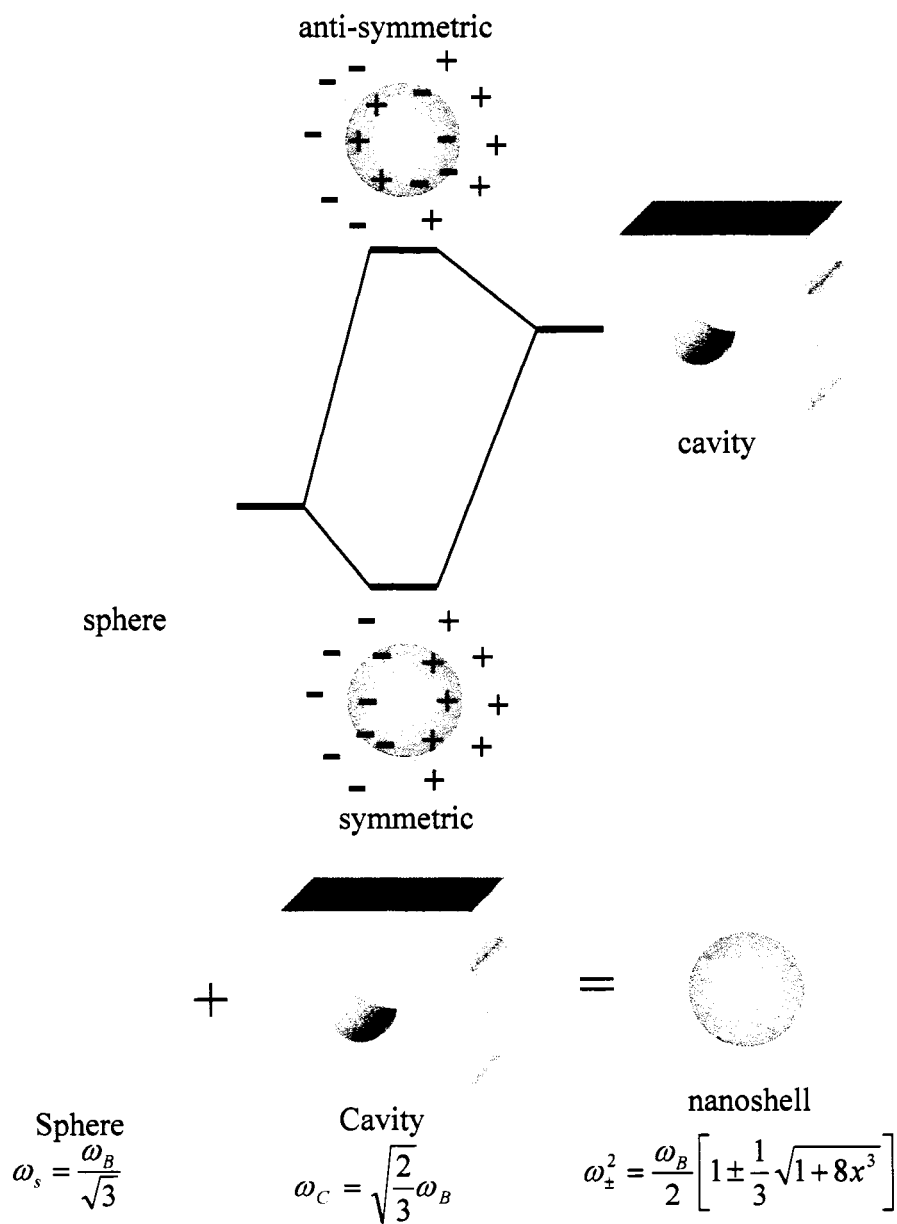


Figure 2.1 Plasmon Hybridization for Gold Nanoshells

The plasmon hybridization model is a mesoscale electromagnetic analog of the molecular orbital theory used to predict how atomic orbitals interact to form molecular orbitals. The plasmon hybridization model separates complex particles into simpler constituent parts and calculates the interaction between the plasmons of the individual parts. For a gold nanoshell, the plasmon hybridization model calculates the interaction between the plasmon of the constituent spherical gold particle (outer nanoshell surface) and a spherical gold cavity (inner nanoshell surface). Figure 2.1 shows a schematic of the plasmon hybridization of the particle and cavity plasmons to form symmetric and antisymmetric plasmon resonances.

The tunability of nanoshells arises from the change in the strength of the interaction between the two plasmons as the thickness of the shell (interaction distance) changes. For a thinner shell the interaction between the two plasmons increases leading to a greater splitting between the symmetric and anti-symmetric plasmon modes. Experimentally only the lower energy symmetric mode is observed due to a difference in the induced dipole, further damped by interband transitions in gold.

2.3 Theoretical Basics of Light Scattering by Nanoshells

Early in the 20th century, Gustav Mie developed the analytical solution of light scattering by a dielectric sphere²². Fifty years later, Aden and Kerker further expanded Mie scattering theory to include particles with core-shell structures³⁷. In the quasi-static limit, for very small particles (diameter $\ll \lambda$), the analytical solution is significantly simplified. For realistic metal nanoshells, the particle sizes lie well outside this quasi-static limit and the simplified Mie scattering theory does not completely describe the plasmon line shape and position. More recently Sarkar et al. developed a vector basis

formalism that is used to model the nanoshell response to an incident plane wave^{39, 40}. The advantages of this formalism over other solutions are that this formalism is valid outside the quasi-static limit and is not computationally intensive. The accuracy of the results has been extensively validated by comparison to experimental data in the laboratory.

The electromagnetic problem of light scattering by nanoshells consists of a plane wave scattering off a spherical nanoshell. In the vector basis formalism the electric and magnetic fields associated with the incident plane wave, and the different layers of a nanoshell are written in terms of the spherical harmonic functions. By satisfying Maxwell's equations at the interfaces between the core and shell and between the shell and embedding medium the scattering coefficients for the electric and magnetic fields can be completely determined.

In a linear, isotropic medium with no external sources and therefore no divergence of the electric field, the general diffraction equation takes on the form of the vector Helmholtz equation

$$\nabla \times \nabla \times \mathbf{G} - \omega^2 \mu \epsilon \mathbf{G} = 0 \quad (2.1)$$

where ω is the angular frequency and ϵ is the dielectric function and μ is magnetic permeability. The electromagnetic fields of the incident wave, scattered wave, and the wave inside the particle can in general, be written as a series expansion of the spherical harmonic basis vectors (\mathbf{M} , \mathbf{N} , \mathbf{L}). The explicit forms and expansion of the electric and magnetic field in the vector harmonic basis along with their orthogonality and completeness is discussed in detail elsewhere⁴⁰. The orthogonality and completeness

implies that any electric or magnetic field can be expressed as a series in terms of the spherical vector basis functions.

$$\mathbf{E} = \sum_{mn} \{a_{mn} \mathbf{M}_{mn} + b_{mn} \mathbf{N}_{mn} + c_{mn} \mathbf{L}_{mn}\} \quad (2.2)$$

Similarly, the magnetic field expansion can be written. Since the divergence is assumed to be zero the solution can be expressed only in terms of the M and N basis vectors functions and c_{mn} must be zero. Thus determining the values of the coefficients (a_{mn} , b_{mn}) completely describes the fields.

2.4 Series Expansion of Incident Plane Wave

The incident plane wave is assumed to be propagating along the z-axis and is linearly polarized in the x direction with unit intensity. This simplifies the form of the expansion coefficients. The scattering coefficients a and b are given by

$$a_{1n} = b_{1n} = i^{n+1} \frac{2n+1}{2n(n+1)}$$

$$a_{-1n} = b_{-1n} = n(n+1)a_{1n} \quad (2.3)$$

and the incident fields can be expressed as

$$E_i = \sum_{n=1}^{\infty} \{a_{\pm 1n} M_{\pm 1n}^{(3)j} + b_{\pm 1n} N_{\pm 1n}^{(3)j}\}$$

$$H_i = -i \sqrt{\frac{\epsilon_3}{\mu_3}} \sum_{n=1}^{\infty} \{a_{\pm 1n} M_{\pm 1n}^{(1)j} + b_{\pm 1n} N_{\pm 1n}^{(1)j}\} \quad (2.4)$$

2.5 Series Expansion for the Nanoshell

For light scattering from a nanoshell, the electromagnetic fields must satisfy Maxwell's boundary conditions at each layer boundary. Figure 2.2 is a schematic of a

nanoshell showing the variable parameters in a nanoshell and the regions where the fields are evaluated. The dielectric core of radius r_1 and dielectric constant ϵ_1 forms region 1. This is coated with a metal layer (typically gold in these experiments) of thickness $r_2 - r_1$ and dielectric constant ϵ_2 and forms region 2. The embedding medium (typically an aqueous medium in these experiments) of dielectric constant ϵ_3 forms region 3.

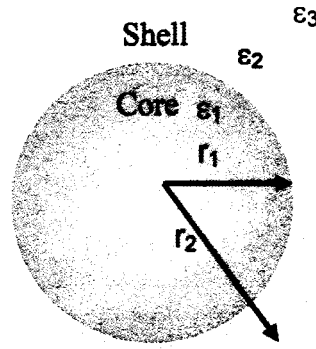


Figure 2.2 : Schematic of a Nanoshell Showing the various parameters

For a spherical nanoshell, with the plane wave incident field defined in equation 2.3 and 2.4, only the \mathbf{M} and \mathbf{N} basis vectors are needed for a complete expansion of the fields. The electric fields are expressed as a series solution of the vector harmonics in the 3 regions as

$$\begin{aligned}
 \mathbf{E}_1 &= \sum_{n=1}^{\infty} \left\{ a_{\pm 1n}^{(1)j} \mathbf{M}_{\pm 1n}^{(1)j} + b_{\pm 1n}^{(1)j} \mathbf{N}_{\pm 1n}^{(1)j} \right\} \\
 \mathbf{E}_2 &= \sum_{n=1}^{\infty} \left\{ a_{\pm 1n}^{(2)j} \mathbf{M}_{\pm 1n}^{(2)j} + b_{\pm 1n}^{(2)j} \mathbf{N}_{\pm 1n}^{(2)j} + a_{\pm 1n}^{(2)h} \mathbf{M}_{\pm 1n}^{(2)h} + b_{\pm 1n}^{(2)h} \mathbf{N}_{\pm 1n}^{(2)h} \right\} \\
 \mathbf{E}_3 &= \sum_{n=1}^{\infty} \left\{ a_{\pm 1n}^{(3)h} \mathbf{M}_{\pm 1n}^{(3)h} + b_{\pm 1n}^{(3)h} \mathbf{N}_{\pm 1n}^{(3)h} \right\}
 \end{aligned} \tag{2.5}$$

and the magnetic fields can be expressed as

$$\begin{aligned}
\mathbf{H}_1 &= -i \sqrt{\frac{\epsilon_1}{\mu_1}} \sum_{n=1}^{\infty} \left\{ a_{\pm 1n}^{(1)j} \mathbf{M}_{\pm 1n}^{(1)j} + b_{\pm 1n}^{(1)j} \mathbf{N}_{\pm 1n}^{(1)j} \right\} \\
\mathbf{H}_2 &= -i \sqrt{\frac{\epsilon_2}{\mu_2}} \sum_{n=1}^{\infty} \left\{ a_{\pm 1n}^{(2)j} \mathbf{M}_{\pm 1n}^{(2)j} + b_{\pm 1n}^{(2)j} \mathbf{N}_{\pm 1n}^{(2)j} + a_{\pm 1n}^{(2)h} \mathbf{M}_{\pm 1n}^{(2)h} + b_{\pm 1n}^{(2)h} \mathbf{N}_{\pm 1n}^{(2)h} \right\} \quad (2.6) \\
\mathbf{H}_3 &= -i \sqrt{\frac{\epsilon_3}{\mu_3}} \sum_{n=1}^{\infty} \left\{ a_{\pm 1n}^{(3)h} \mathbf{M}_{\pm 1n}^{(3)h} + b_{\pm 1n}^{(3)h} \mathbf{N}_{\pm 1n}^{(3)h} \right\}
\end{aligned}$$

The superscripts represent the region and the type of the scattering coefficient. The region that includes the origin (region 1) only has radial contributions from the spherical Bessel functions (j); regions that are not bounded (region 3) contain only the Hankel functions of the first kind (h). Region 2 has contributions from both types of functions. Assuming that the materials are nonmagnetic so that the relative permeability $\mu=1$ simplifies the above equations. With the fields given in equations 2.4, 2.5 and 2.6 matching the transverse electric and magnetic fields at the two boundaries yields 8 equations with 8 unknown coefficients. These can be solved to completely determine the electric and magnetic fields everywhere.

2.6 Nanoshell Far Field Scattering Properties

The far field scattering, absorption and extinction cross-sections of the nanoshells can be determined from the a and b coefficients determined in region 3, in the previous section. The cross-sections in terms of the scattering coefficients are given as

$$\begin{aligned}
\sigma_{sca} &= \frac{2\pi}{k^2} \sum_{n=1}^{\infty} (2n+1) (|a_{1n}^{(3)h}|^2 + |b_{1n}^{(3)h}|^2) \\
\sigma_{ext} &= -\frac{2\pi}{k^2} \text{Re} \sum_{n=1}^{\infty} (2n+1) (a_{1n}^{(3)h} + b_{1n}^{(3)h}) \\
\sigma_{abs} &= \sigma_{ext} - \sigma_{sca}
\end{aligned} \tag{2.7}$$

The extinction cross-section can be easily matched to the experimentally determined absorbance of nanoshells.

2.7 Nanoshell Near Field Scattering

The local near field around the nanoshells is related to the SERS efficiency of the nanoshells. The near field at the surface of the nanoshells is calculated using equation 2.5 in region 3.

$$\mathbf{E}_3 = \sum_{n=1}^{\infty} \left\{ a_{\pm 1n}^{(3)h} \mathbf{M}_{\pm 1n}^{(3)h} + b_{\pm 1n}^{(3)h} \mathbf{N}_{\pm 1n}^{(3)h} \right\} \tag{2.5c}$$

Throughout the rest of the thesis, the near fields at the surface are evaluated at a distance of 0.1 nm from the surface unless otherwise stated. The radial distance is fixed and the surface average is calculated as the average of the field evaluated at 2500 different points on the nanoshell surface (50 different θ and 50 different ϕ angles).

To calculate the nanoshell electric field decay profile, the field is calculated in steps of 0.25 nm in the radial direction. At each step the surface average field is calculated as the average of the field at 2500 different points at that radial distance from the surface.

2.8 Homogeneous and Inhomogeneous Broadening

Implementation of the above discussed vector basis formalism for determining the extinction spectra of nanoshell solutions gives good agreement with the position of the

peak, but the predicted line width is smaller than the experimentally observed spectra. The peak width is affected by three different broadening mechanisms. The first is due to the size dispersion in the core diameter and shell thickness. Even under the best experimental condition, this size distribution is inevitable. It can be minimized to about 5-7 % distribution in the core diameter by careful attention to the purity of the reactants used in the process to make the silica core particles. The second is due to the size of nanoshells. As the total overall size of the nanoshells increases, the wavelength for which the resonance occurs for a given r_1/r_2 ratio increases with an increase in the line width of the plasmon resonance. This is due to phase retardation effects as the nanoshell size becomes comparable to the wavelength of light. The phase retardation of the electric field also excites higher order modes, such as the quadrupole, and octopole, in larger shells. Even though these higher order modes are spectrally separated from the dipole, they also contribute to the broadening of the dipole peak in nanoshells. For most nanoshells with dipole resonance in the visible and near-IR regions, at least 5 multipolar terms of the series are needed to achieve good agreement with the experimental data. For all calculations in this thesis ten terms of the series have been considered so as to include even small variations due to the higher order terms.

The third is due to the inhomogeneity of the shell thickness around the core silica particles. The electroless plating method used to grow the gold shell around the silica particles is a kinetically driven process and may lead to non uniform deposition of gold around the silica particles. Recently Wang et al.⁴¹ have demonstrated that small non uniformities in the shell thickness around the silica particles, which leads to the core particle being offset from the particle center, leads to large variations in the measured

spectrum of single nanoshell particles. For ensemble measurements of the nanoshell particles, the measured spectrum then is an envelope of the spectra of a mixture of perfectly concentric nanoshells and nanoshells with varying degrees of inhomogeneity in the shell thickness.

Nehl et al.⁴² have also demonstrated from single particle measurements that the line width of the bulk nanoshell spectra is broadened due to the inhomogeneity in the particle size, and that other factors have negligible small effect on the dipole line width of nanoshells.

The SERS analysis presented in this thesis is done without consideration of broadening of the line width due to particle size distribution or shell thickness inhomogeneities, i.e. all calculations are for perfectly concentric nanoshells of a given average size. Line width broadening due to phase retardation has been included in all calculations of far field and near field properties of nanoshells.

2.9 SERS Enhancement Calculation

The SERS response of a Raman active molecule attached to a nanoshell is biquadratic with respect to the enhanced near field of nanoshells. This biquadratic term can be further broken down as a product of the excitation field intensity and the Stokes - shifted scattered field intensity. For the SERS measurements, the nanoshells are excited by a laser at a wavelength $\lambda_L = 785$ nm. The SERS response depends on the intensity of the excitation light, the nanoshell plasmon response at the excitation wavelength and the Raman scattered intensity at the Stoke-shifted wavelength. The SERS response is calculated as the surface average of the field at the excitation laser wavelength and the Stoke-shifted wavelength. At the excitation wavelength, the field is due to the laser

($\mathbf{E}_{\text{incident}}(\lambda_L)$) and the nanoshell plasmon response at that wavelength ($\mathbf{E}_{NS}(\lambda_L) = \mathbf{E}_3$). At the emission wavelength the field is due to the nanoshell plasmon response at the Stokes - shifted wavelength. Thus the total SERS response can be written as

$$\mathbf{E}_{SERS} = \left\langle \left| \mathbf{E}_{\text{incident}}(\lambda_L) + \mathbf{E}_{NS}(\lambda_L) \right|^2 \bullet \left| \mathbf{E}_{NS}(\lambda_S) \right|^2 \right\rangle \quad (2.8)$$

where the $\langle \rangle$ brackets denote the averaging over the nanoshell surface.

In the following chapters the SERS response is calculated using Equation 2.9. For the dye molecule fluorescein placed at different distances from the surface the SERS response follows the near field, whereas for the tether adenine molecules the SERS response follows the sum of the field at the position of the molecule.

Chapter 3 : Experimental Considerations and Sample Preparation

3.1 Introduction

The primary goal of this set of experiments is to measure the surface enhanced Raman scattered intensity and the fluorescence intensity of a dye molecule placed at increasing distances from the surface. Placing the dye molecules close to the nanoshell surface is expected to give larger SERS intensity signals, whereas the fluorescence signal would be quenched by the metal surface. Designing the sample geometry to obtain an easily measurable and reproducible signal is important. The system consists of a silica gold nanoshell with a ss-DNA tether which forms a nanoscaffold that allows the dye molecules to be placed at varying distances from the nanoshell surface. The flexibility allowed by the tunability of the nanoshells and the easily varied ss-DNA tether lengths are exploited to map the SERS and fluorescence intensity profile around a nanoshell.

3.2 Silica Gold Nanoshell fabrication

The silica gold nanoshell fabrication technique is based on protocols previously developed by Oldenburg et al.^{30 43}. The silica core is synthesized using the Stöber method⁴⁴ of particle growth. The Stöber method involves the base catalyzed hydrolysis and condensation of tetraethylorthosilicate (TEOS). Typically TEOS and ammonium hydroxide are mixed in varying ratios in ethanol to produce silica nanoparticles in the 80 nm – 250 nm diameter size regime. After the silica particles are synthesized the

surface is functionalized with 3-aminopropyltriethoxysilane (APTES). This chemical functionalization of the silica surface provides an amine moiety at the surface, which is used to attach small gold colloid. For small silica nanospheres (< 90 nm diameter), the functionalization of the surface with APTES leads to a disproportionately large number of aggregates due to polymerization of the APTES. An alternative functionalization of the silica surface is achieved using N-n-Butyl-aza-2,2-dimethoxysilacyclopentane. (Gelest catalog number SIB 1932.4). This molecule does not self polymerize and does not cause aggregates to form during the silanization process. For the SERS experiments nanoshells made on core particles with a diameter of 86 nm were functionalized with this silane molecule.

Small gold colloid particles 1-3 nm in size are synthesized by reducing chloroauric acid using tetrakis(hydroxymethyl)phosphonium chloride (THPC) as a reducing agent. The THPC-Au attached to the silica surface act as nucleation sites for the electroless deposition of Au to form a complete shell on the silica core. The electroless deposition was achieved by reducing gold from a solution of 1.8 mM potassium carbonate and 0.4 μ M chloroauric acid by formaldehyde. The growth of a complete shell is monitored by UV-Visible spectroscopy.

Most of the silica cores used for these experiments were synthesized in the laboratory using the procedure outlined above. Silica nanospheres used as core particles are also commercially available. Small silica particles (diameter = 86 nm) were received as a sample from Precision Colloid (precisioncolloid.com).

3.3 Nanoshells for SERS Experiments

Tuning the individual nanoshell plasmon resonance position to the excitation laser wavelength results in a SERS enhancement, which follows the individual nanoshell response⁶. The measured and calculated SERS response is maximized when the single nanoshell electromagnetic response is tuned to spectrally overlap both the excitation and Stokes-shifted frequencies. To design nanoshells for surface enhanced Raman scattering experiments, nanoshells with a resonance tuned close to the excitation laser wavelength were made. The Raman modes studied are at a Raman shifted frequency 736 cm^{-1} (833 nm) and 1185 cm^{-1} (865 nm) for adenine and fluorescein, respectively. The Renishaw Invia Raman spectrometer used in these experiments has a excitation laser at 785 nm. Therefore the nanoshells were designed with a dipole plasmon resonance at 800 nm in water. Nanoshells with a core radius of 70 nm and a shell thickness of 21 nm (dimensions $[r_1, r_2] = [70, 91]\text{ nm}$) were made to achieve a dipole resonance at 800 nm.

Figure 3.1 shows the extinction spectrum (far field response) of the $[r_1, r_2] = [70, 91]\text{ nm}$ nanoshells in black. The red line indicates the excitation laser at 785 nm, the blue line indicates the wavelength at which the Stokes-shifted symmetric stretching mode of the adenine molecule is observed, and the green line indicates the wavelength for the Stokes-shifted Raman mode for fluorescein. The linewidth of the dipole resonance of the nanoshells is sufficiently broad to cover the excitation laser and both the Stokes-shifted Raman modes. Figure 3.1 also includes the calculated surface average $|E|^4$ spectrum (in red). This is a measure of the efficiency of the nanoshells for SERS. The peak position of this spectrum is red shifted with respect to the extinction spectrum by $\sim 150\text{ nm}$. Thus the

SERS response is detuned from the wavelength corresponding to the peak of the near field response.

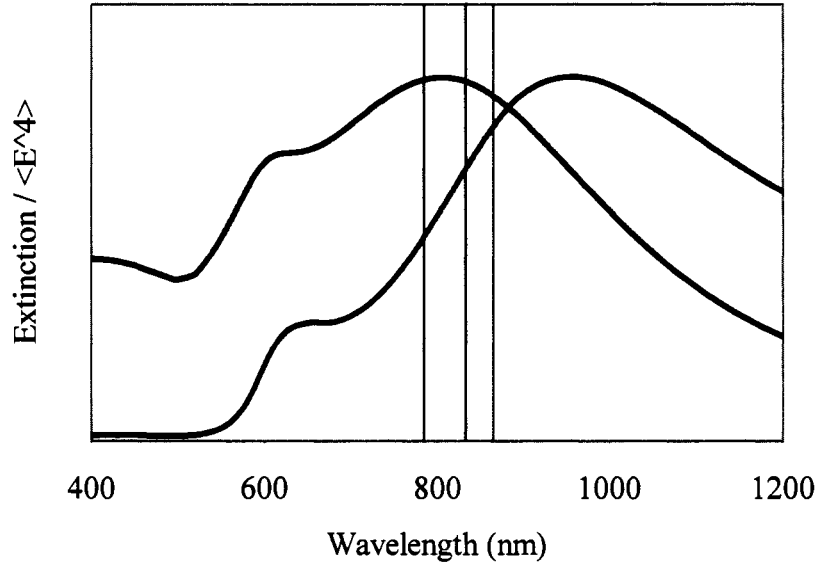


Figure 3.1 : Far field spectrum (black) and the calculated surface average near field spectrum (red) for $[r_1, r_2] = [70, 91]$ nm nanoshells. The excitation laser at 785 nm (red line), the emission peak wavelengths for the adenine (blue) and fluorescein (green) are included. The spectra are scaled for clarity.

The second set of nanoshells used in these experiments was designed such that the SERS response is tuned to the excitation laser wavelength and both Raman Stokes-shifted modes. Nanoshells of dimensions $[r_1, r_2] = [43, 58]$ nm were synthesized with a dipole SERS response tuned to the excitation laser wavelength. Figure 3.2 shows the extinction spectrum (in black) and the calculated surface average $|E|^4$ (in red) for these nanoshells. Lines indicating the pump laser wavelength at 785 nm (red line), and the wavelengths at which the Stokes-shifted modes of the dye molecule fluorescein (green line) and adenine

(blue line) are again included for reference. As can be seen in Figure 3.2, the near field dipole peak is tuned to the excitation laser, but the far field extinction spectrum (in black) is highly detuned from the excitation laser.

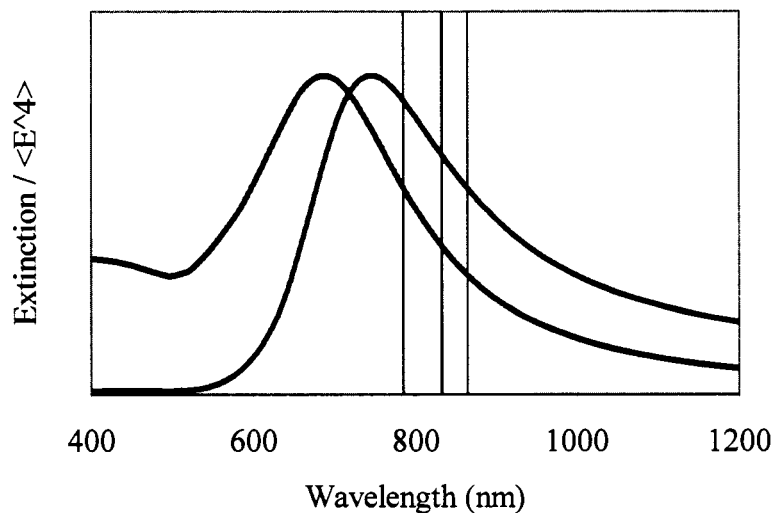


Figure 3.2 : Extinction spectrum (black) and the calculated surface average near field spectrum (red) for $[r_1, r_2] = [43, 58]$ nm nanoshells. The excitation laser at 785nm (red line), the stokes emission peak wavelengths for the adenine (blue) and fluorescein (green) are included. The spectra are normalized for clarity.

3.4 Nanoshells for Fluorescence Measurements

The fluorescence experiments were carried out on nanoshells in aqueous solution. The fluorescent dye molecule used is fluorescein that has an absorption maximum at 495 nm and an emission maximum at 520 nm. Figure 3.3 shows the extinction spectrum of the nanoshells used in the fluorescence experiments. The nanoshells have dimensions of $[r_1, r_2] = [70, 88]$ nm. The absorption and emission wavelengths of fluorescein are included

for reference. The emission maximum of fluorescein is in a region where the nanoshells do not absorb very efficiently. Thus absorption of the fluorescence emission by the nanoshells is minimized. The nanoshells primarily act as a metal surface that quenches the fluorescence emission from the fluorescein. The enhancement of the absorption is also small in this region.

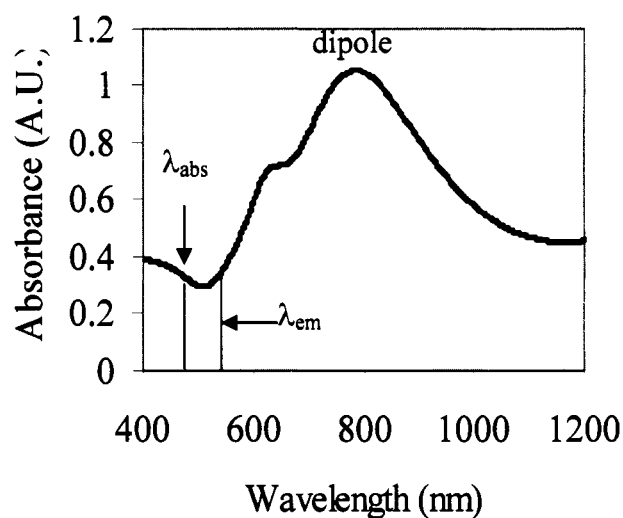


Figure 3.3 : Absorbance spectrum of nanoshells used for fluorescence measurements.

The absorption and emission maximum wavelengths for fluorescein are included.

3.5 ss-DNA as Tether for Building a Nano-scaffold

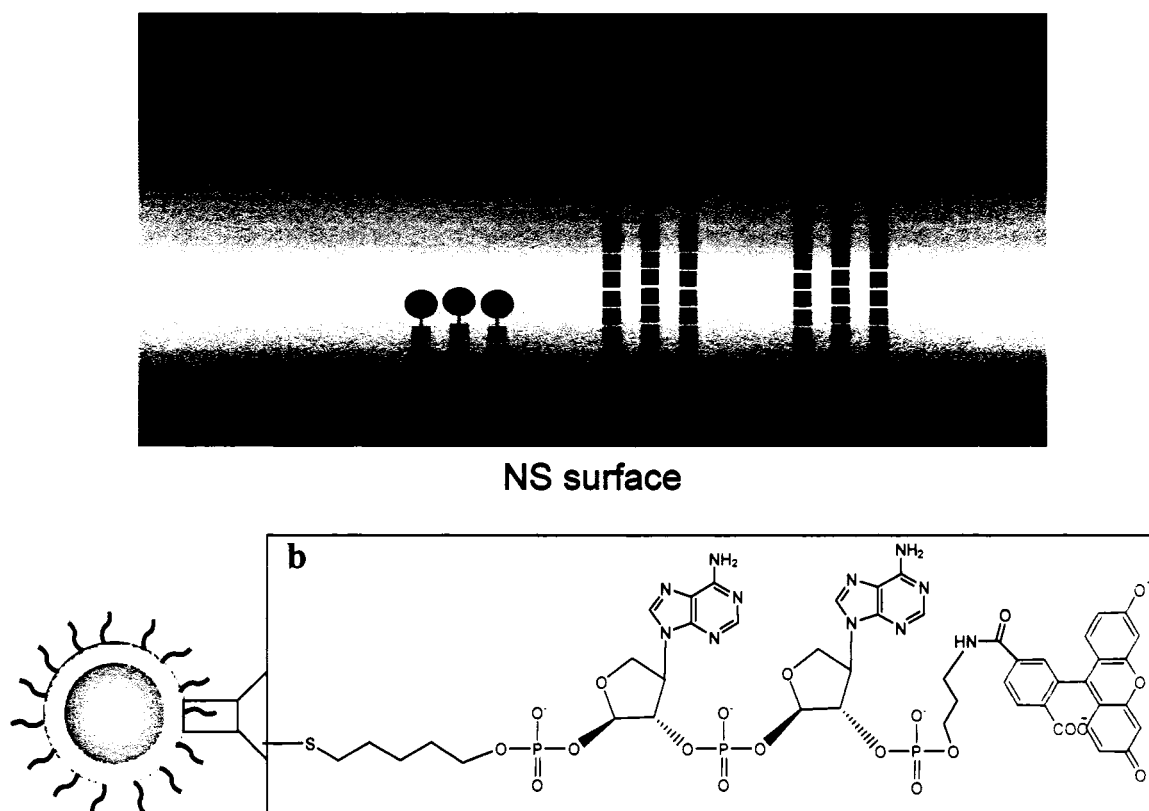


Figure 3.4 : a) Schematic illustrating the different lengths of the ss-DNA nano-scaffold used to place the fluorescein at different places in the near field of the nanoshell. b) Schematic of the thiolated ss-DNA-fluorescein conjugate structure with 2 adenine bases.

For both the SERS measurements and the fluorescence experiments the fluorescein dye molecule is placed at varying distances from the nanoshell surface using single stranded DNA (ss-DNA) oligonucleotide strands. Figure 3.4 is a schematic illustrating the placement of the fluorescein molecule at different distances from the nanoshell to interrogate the varying field intensity. The ss-DNA used for these experiments are bifunctional oligonucleotides. 6-Carboxyfluorescein is attached to the 3' end of the ss-DNA via a 6-carbon chain spacer. A schematic structure of the bi-functional

oligonucleotide used is shown in Figure 3.4 b. As can be seen in Figure 3.5, the fluorescein molecule attached to a ss-DNA has an absorption maximum at 494 nm and an emission maximum around 520 nm.

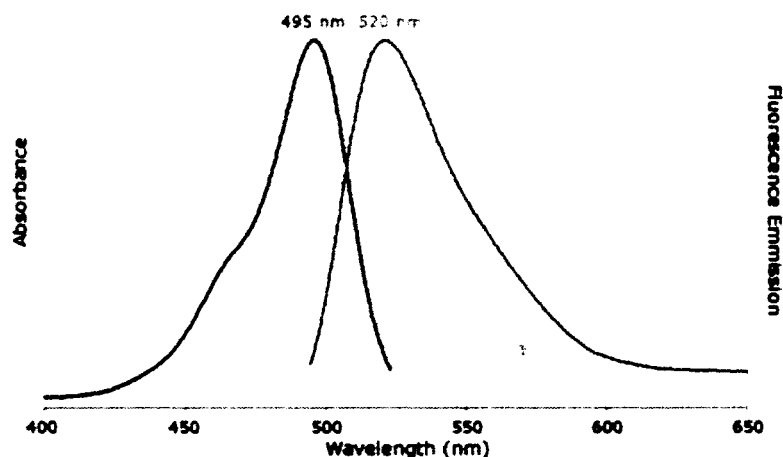


Figure 3.5 : Absorption and emission spectra of fluorescein at pH 8.5

The 5' end of the ss-DNA has a thiol modification attached via a 6 carbon spacer. The thiol modification is a di-sulphide bridge, which must be cleaved before the thiol is available for attaching to the gold nanoshell surface.

The thiol-gold affinity provides an easy method to conjugate the ss-DNA to the nanoshell surface. The number of bases in the ss-DNA determines the length of the tether. The number of bases in the tether can be easily varied in steps to change the distance between the nanoshell surface and the fluorescein molecule in a controlled fashion. The reduced thiol adds ~ 1.2 nm to the length of the ss-DNA while the 6-FAM adds ~ 2.1 nm. Each base adds about 0.68 nm to the length of the DNA. This is consistent with the length scales reported by Parak et. al.⁴⁵ The confirmation of ss-DNA attached to gold colloid has been extensively studied^{45, 46}. For short ss-DNA attached to gold colloid,

the ss-DNA assumes a radially stretched confirmation. For longer ss-DNA, i.e. lengths greater than 30 bases, the ss-DNA assumes a partially stretched and partially coiled confirmation. For the SERS experiments ss-DNA of length 2 to 18 bases were used. These were assumed then to be in a radially stretched confirmation. The lengths used for the fluorescence measurements consist of 6 to 36 bases. A mixed SAMS of ss-DNA and mercaptohexanol ensures the radially stretched confirmation for ss-DNA nanoshell conjugates in solution. Formation of the mixed SAMs of ss-DNA and mercaptohexanol is discussed in a later section of this chapter.

The oligonucleotide bases have strong absorbance in the UV region around 260 nm. Thus there is minimal fluorescence background from the tether molecules when fluorescein is excited at 494 nm. For the SERS measurements only adenine bases were used in the tether. The ring structures of the oligonucleotide bases are all Raman active. The Raman peaks from the various bases would make the SERS spectra complicated without providing any further useful information. Adenine base was chosen for the tether in the SERS measurements because adenine has low nonspecific binding to gold surfaces, its SERS spectra has been previously characterized and, verified mode assignments are available^{16, 47-49}. Guanine was rejected as more than 4 guanine bases together forms self-complementary tetraplex structures that are extremely stable and so radially stretched confirmation was not feasible. Cytosine and guanine were not used as they are known to modify the fluorescence properties of fluorescein attached directly these bases.

The ss-DNA attached to the gold surface can also be completely displaced from the surface by the addition of mercaptoethanol⁵⁰. This short alkanethiol displaces the ss-

DNA on the surface by a thiol displacement reaction⁵¹. The surface coverage of the ss-DNA on the nanoshell can then be quantified by fluorescence spectroscopy.

3.6 ss-DNA Sequences used for the SERS and Fluorescence

Measurements

A list of all sequences used for the SERS and fluorescence experiments is shown in Table 3.1. The 5' end of the sequences has a 6-carbon (CH₂)₆ spacer between the thiol moiety and the first nucleotide. The 3' end is modified with 6-FAM fluorescein modification. The mixed base sequences for the fluorescence experiments were analyzed to prevent self-hybridization and formation of hairpin bends in the sequences. Other than those considerations the exact sequences are irrelevant to the measurement.

Table 3.1: List of DNA sequences used for the SERS and fluorescence experiments.

Sequences used for fluorescence measurements

Name of Sequence	Sequence (5'-3')
6mer-6FAM	CAG GAT-F
12mer-6FAM	CGC ATT CAG GAT-F
24mer-6FAM	CGC ATT CAG GAT CGC ATT CAG GAT-F
36mer-6FAM	CGC ATT CAG GAT CGC ATT CAG GAT CGC ATT CAG GAT-F

Sequences used for SERS experiments

2A-6FAM	AA-F
6A-6FAM	AAA AAA-F
12A-6FAM	AAA AAA AAA AAA-F
18A-6FAM	AAA AAA AAA AAA AAA-F

3.7 Cleaving and Desalting the ss-DNA

ss-DNA used for both the SERS and fluorescence experiments were purchased from Integrated DNA technologies Inc. (idtdna.com) or Oligoset Inc. (oligoset.com). Thiolated oligonucleotides used in these experiments were received as lyophilized disulphides. Before use the disulphide bridge had to be cleaved and the residual part of the modifier removed from the solution. The disulphide is cleaved by dissolving the lyophilized oligonucleotide in 300µl of 100 mM solution of dithiothreitol (DTT) (Sigma-Aldrich) in a 0.1M sodium phosphate pH 8.3 buffer. This reaction was allowed to proceed for 1 hour at room temperature. The short organic thiol cleaved from the oligonucleotide, was removed by elution down a Sephadex25 NAP-5 column (Amersham Biosciences) using 600µl milliQ water (water purified to resistivity > 18Ω. by milliQ system by Millipore Corp.) The purified solution was quantified by measuring the absorbance at 260nm on a Cary 5000 spectrophotometer. (Varian Inc.) The absorbance at 260nm is related to the concentration by

$$\text{Concentration} = A_{260} * d / E \quad (3.1)$$

where d is the dilution factor and E is the extinction coefficient specific to each sequence. Purified oligonucleotide was stored at -20° C until use.

3.8 Preparation of Nanoshell-ss-DNA conjugates for SERS experiments

Fused quartz slides were cleaned in piranha solution (7:3 v/v 98% H₂SO₄ : 30% H₂O₂) at 70°C for 30 minutes, rinsed in milliQ water, followed by a rinse with 200 proof ethanol and dried in a stream of dry N₂. (*Note: piranha is a strong oxidizing agent and extremely hazardous.*) The surface of the quartz slides were then functionalized with

poly-(4 vinyl)-pyridine (PVP), by dip coating the slides in a 1% PVP solution in ethanol for 2 hours⁵². The slides were removed from the PVP solution and rinsed in 200 proof ethanol to remove any loosely bound PVP from the slides. The PVP coating was allowed to cure overnight at room temperature. Next adhesive spacer masks (Secure Seal, Molecular Probes) were applied to the slides to form 20mm diameter x 0.12mm deep wells. 300 μ l of nanoshells solution (absorbance \sim 1.5 at the dipole peak) prepared the same day was placed in each well and allowed to incubate for at least 2 hours. The excess nanoshell solution was removed. Before the nanoshell film could dry out, 250 μ l of 40 μ M oligonucleotide solution was added to each well. This was allowed to incubate for 48 hours in the dark. The excess solution was then pipetted off. The samples were gently rinsed once by adding 250 μ l of milliQ water to each sample spot and removing the milliQ water by pipette. Note that the conjugation of the ss-DNA to nanoshells is best when the nanoshells are made the same day as the conjugation is carried out. Conjugating the ss-DNA to nanoshells prepared more than a day earlier leads to extremely poor attachment. Figure 3.4 is an optical microscope image of the nanoshells immobilized on the quartz slide.

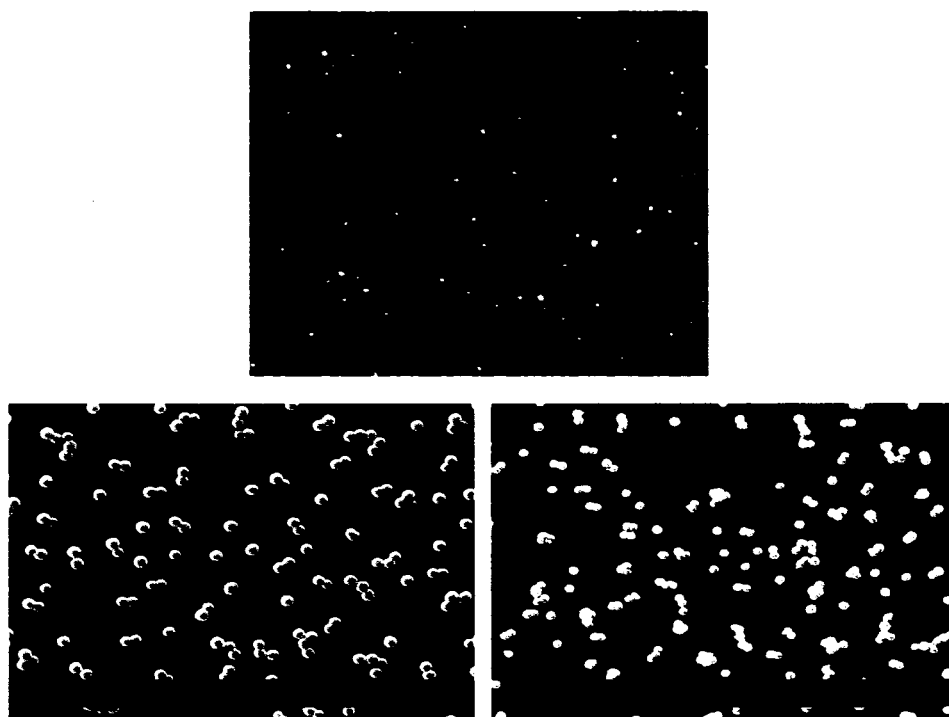


Figure 3.6: (Top) Dark field image of nanoshell-DNA conjugates immobilized on quartz slides. (Bottom) SEM images of nanoshell-DNA conjugates immobilized on quartz slides (left) $[r_1, r_2] = [70, 91]$ nm shells and (right) for $[r_1, r_2] = [43, 58]$ nm nanoshells

SERS measurements were carried out on the Renishaw inVia micro Raman spectrometer using a 63X water immersion objective. The micro Raman spectrometer is equipped with a 785 nm diode laser that was used as the excitation laser for the SERS experiments. The laser power used for all the experiments was about 55 μ W (0.1% transmission with no filter) at the sample, in a 30 μ m x 3 μ m spot size. Collection times varied between 30 seconds (for the larger nanoshells, $[r_1, r_2] = [70, 91]$ nm) to 60 seconds (for the smaller nanoshells, $[r_1, r_2] = [43, 58]$ nm). All measurements were carried out in solution at pH 9.2.

3.9 Nanoshell ss-DNA conjugates for fluorescence measurements

Figure 3.5 is a schematic representation of the steps involved in making the ss-DNA-nanoshell conjugates for the fluorescence measurements. The ss-DNA nanoshell

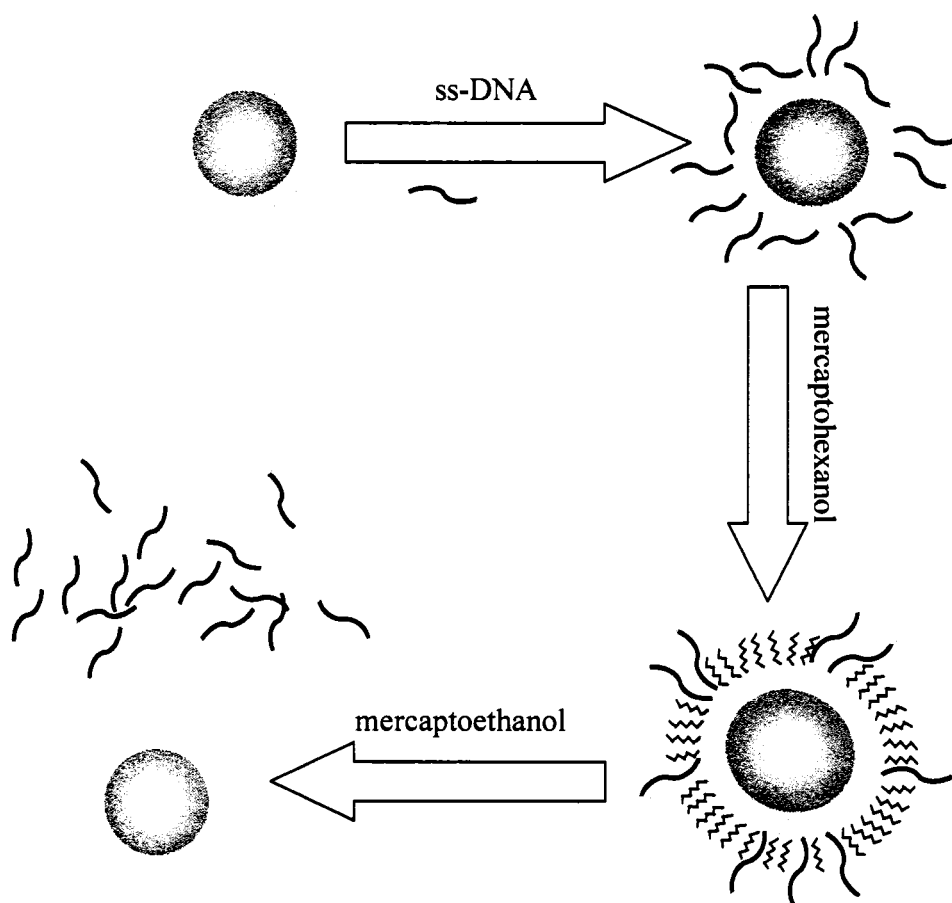


Figure 3.7: Schematic illustrating the steps involved in fabricating nanoshell-DNA-MCH conjugate structures for fluorescence measurements.

conjugates for the fluorescence experiments were made in solution. 50 μ l of 100 μ M oligonucleotide solution was added to 950 μ l of nanoshell solution in an 1.7 ml eppendorf tube. The samples were then covered in foil and allowed to incubate at room temperature for 48 hours. Covering the samples prevents undesirable photobleaching of the

fluorophore by sunlight and overhead room lights. The excess ss-DNA was then removed from solution by centrifuging and redispersed it in water at least twice.

3.10 Mixed ss-DNA and Mercaptohexanol layers on Nanoshells

The thiol gold bond is strong and thermodynamically stable. Ideally the ss-DNA would attach to the gold surface of the nanoshells via the thiol moiety. Along with gold thiol conjugation, there is some non-specific binding between the various nucleotide bases and the nanoshell gold surface. To remove the non-specifically bound DNA and leave only the strands bound to the surface by the thiol linker, the nanoshells are redispersed in a 1 μ M solution of mercaptohexanol for 1 hour in the last centrifugation cycle^{46, 53, 54}. Tarlov et al. have demonstrated that the co-adsorption of mercaptohexanol on Au surfaces with ss-DNA SAMs have the effect of displacing the oligonucleotide bases bound to the Au surface and forming a dense sublayer. Mercaptohexanol is the same chain length as the spacer used to attach the ss-DNA via the thiol moiety to the Au surface. The hydroxyl group at the end makes MCH more hydrophilic. The remaining ss-DNA are bound only through the thiol linkage. The sublayer also prevents the oligonucleotide bases from further contact with the gold surface and promotes the radially stretched configuration of the ss-DNA strands. Centrifuging and redispersing the nanoshells in water removed the excess mercaptohexanol.

It is important to determine the concentration and amount of mercaptohexanol required to remove the nonspecifically bound oligonucleotide without displacing the ss-DNA bound to the surface via the thiol bond. Too much excess mercaptohexanol can aggregate the nanoshell solutions. If the ss-DNA nanoshell conjugates are left in the mercaptohexanol for a long time, the mercaptohexanol can completely displace the ss-

DNA bound via the thiol bond. Towards this end nanoshell solutions can be dispersed in a series of mercaptohexanol solutions of various dilutions. Typically 950 μl of nanoshell solution (of similar concentration as that used to make the ss-DNA nanoshell conjugates) are spun down and then redispersed in 1ml of mercaptohexanol solution of different concentrations in water. The UV-Visible absorbance spectra of the solutions are then monitored to avoid concentrations of mercaptohexanol that aggregate the nanoshell solutions. For the samples made for this set of fluorescence experiments a 1 μM mercaptohexanol for 1 hour was optimal.

3.11 Quantifying the surface coverage of ss-DNA on Nanoshells

The mercaptohexanol is removed from solution by centrifuging and redispersing the samples in sodium phosphate buffer pH 8.3. After the second centrifuge cycle the nanoshell conjugates were redispersed into 500 μl of buffer. The final volume of the ss-DNA coated nanoshells was then split into 2 equal volumes. The first volume was used to measure the fluorescence intensity with the fluorescein molecules tethered to the nanoshell surface and measure the absorbance of each sample to determine the concentration of the final solution. This helps compensate for nanoshells that may be lost during the numerous centrifuge cycles and also helps determine if any samples have aggregated. To the second volume of the solution, 250 μl of a 12mM mercaptoethanol solution in water was added to displace the DNA attached to the nanoshells via a thiol displacement reaction⁵⁰. The mercaptoethanol was allowed to react for at least 12 hours. Centrifuging the solution (\geq twice the speed used to normally centrifuge the DNA: NS solution) pulls all the nanoshells out of the solution and the concentration of the

untethered DNA in the supernatant solution was determined by fluorescence spectroscopy.

3.12 Conclusion

Design of nanoshells for the SERS and fluorescence experiments and sample geometry considerations for both measurements are outlined in this chapter. For SERS experiments using the Renishaw inVia micro Raman spectrometer, nanoshells tuned to the laser were designed and immobilized on fused quartz slides. The nanoshells were immobilized for the SERS experiments to prevent absorption of the Raman scattered light. This also allows for easy focusing on the nanoshells and making reproducible samples. For the fluorescence measurements, longer DNA strands were used. A mixed SAM of ss-DNA and mercaptohexanol on nanoshells was created to reduce non-specific attachment of the DNA to nanoshells and preferentially leave DNA in a radially stretched configuration. This mixed SAM of ss-DNA and MCH on nanoshells also improve the reproducibility of the measurements.

Chapter 4 : SERS and Fluorescence Results

4.1 Introduction

Theoretical prediction of the spatial extent of the near field of a nanoshell using Mie scattering theory shows a large enhancement of the incident field very close to the nanoshell surface that decreases as the distance from the nanoshell surface increases. The surface enhanced Raman scattering (SERS) intensity is strongly related to the near field intensity as approximately E^4 (Equation 2.9). The absorption and emission are both dependent on the intensity of the near field.

$$E_{SERS} = \left\langle \left| \mathbf{E}_{incident}(\lambda_L) + \mathbf{E}_{NS}(\lambda_L) \right|^2 \bullet \left| \mathbf{E}_{NS}(\lambda_S) \right|^2 \right\rangle \quad (2.9)$$

Therefore it is predicted that the SERS intensity will decrease as a Raman active molecule is placed at increasing distances from the surface of a nanoshell. On the other hand fluorophores placed very close to a metal surface have additional nonradiative decay paths that quench their fluorescence intensity. This quenching effect is most pronounced very close to the surface (a few nm from the surface) and falls off as the separation between the fluorophores and metal surface increases. At larger distances from the surface, there is an enhancement in the fluorescence intensity due to the near field enhancement around nanoshells. The enhancement may extend up to tens of nm from the metal surface^{18, 19}.

This chapter outlines the results of experiments designed to map out the near field decay using SERS and fluorescence spectroscopy. In this chapter the discussion of the results are structured as follows: In section 4.2 the SERS experiments with DNA scaffolds are discussed. The investigations were performed for two different sets of nanoshells immobilized on fused quartz slides. The first set of nanoshells is designed with the far field dipole response tuned to the excitation laser. The second set of nanoshells is designed with the near field dipole response tuned to the excitation laser. The figures for both sets of nanoshells are presented side by side, and the experimental details and discussions are valid for both sets of nanoshells. Section 4.3 details the results of the fluorescence experiments performed to determine the packing density of the ss-DNA on nanoshells as well as the quenching or enhancement of the fluorescence intensity when the fluorescein molecule is tethered to the nanoshells. These measurements were correlated with the theoretically calculated near field intensity.

4.2 Surface Enhanced Raman Scattering from ss-DNA-Nanoshell

Conjugates

Figure 4.1 is a schematic representation of the thiolated polyadenine scaffold with a terminal fluorescein moiety attached to the surface of a gold nanoshell as previously described in Section 3.4. The Raman active parts of this conjugate structure whose intensity varies with changing distance from the nanoshell surface are the fluorescein molecule and the adenine ring structure. The SERS experiments were carried out using ss-DNA with 2, 6, 12, and 18 adenine molecules per strand.

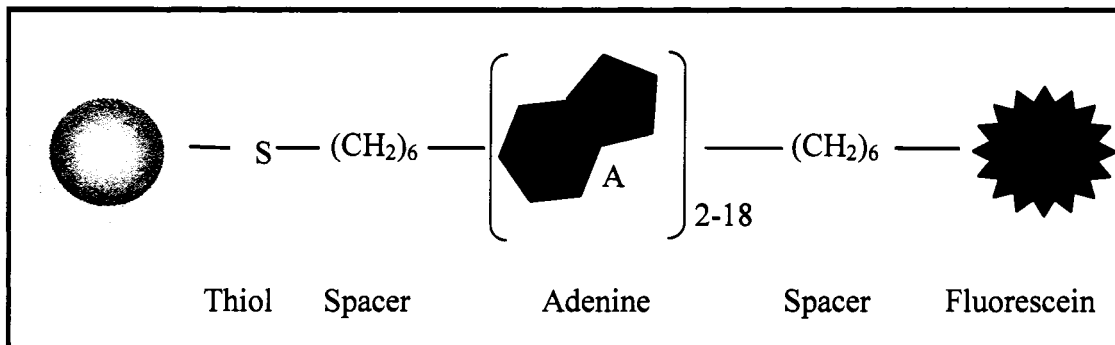


Figure 4.1 : Schematic representation of the adenine-fluorescein conjugate structure attached to a nanoshell (not to scale). The adenine and fluorescein moieties are accurately depicted in Figure 3.4

Figure 4.2 shows representative SERS spectra of the fluorescein-adenine conjugates attached to the 2 different sets of nanoshells as describes previously in section 3.3. Each spectrum is the average of 10-12 spectra taken at different spots on the sample. The spectra are normalized by matching the region between 1700 cm^{-1} and 2100 cm^{-1} (minimizing the least square difference between the 4 spectra) to account for the variation in nanoshell density in the laser spot. In this region (not shown) there are no contributions from the adenine and fluorescein moieties and the background is only from the nanoshells and substrate. The SERS spectra in figure 4.2 show a large number of peaks with significant overlap of several adenine and fluorescein peaks.

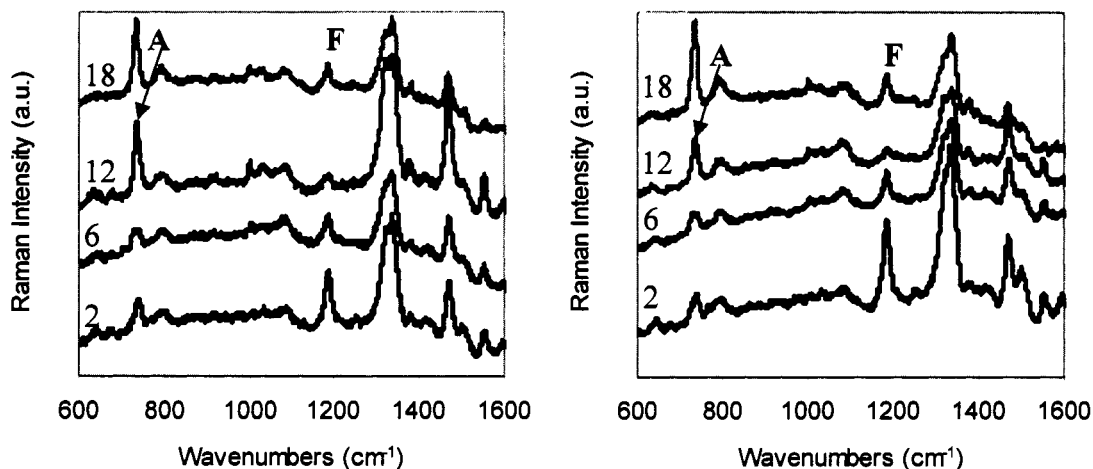


Figure 4.2: SERS spectra for the 4 lengths of adenine strands (left) nanoshell extinction tuned to the excitation laser (70-91 nm) and (right) nanoshell near field tuned to the pump laser (40-58 nm). The number of adenine moieties in the scaffold molecules is indicated on the left of each spectrum.

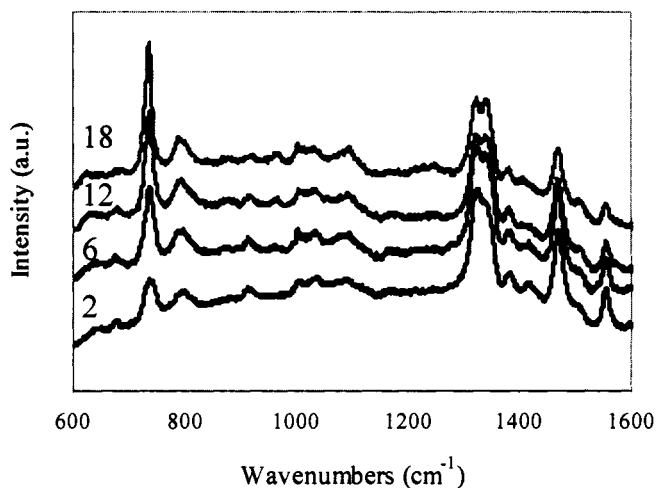


Figure 4.3: SERS spectra of adenine strands (without fluorescein) on the $[r_1, r_2] = [70, 91]$ nm size nanoshells. Number of adenine moieties per molecule in the scaffold molecules is indicated on the left of each spectrum.

The peak assignments were obtained by comparison with literature references^{16, 47-49, 55} and from SERS experiments performed using pure fluorescein deposited on nanoshells⁵⁶ and thiolated adenine attached to nanoshells. Figure 4.3 shows representative SERS spectra for the thiolated adenine.

Further analysis is based on the 736cm^{-1} peak, attributed to a symmetric stretching mode of the adenine ring, and the 1185 cm^{-1} CCH bending mode of fluorescein. These two modes are marked A and F, respectively, in Figure 4.2. The remaining peaks can be assigned to adenine or fluorescein but are not used in the present analysis because either the adenine and fluorescein peaks strongly overlap each other (e.g. the double peak at $\sim 1330\text{ cm}^{-1}$) or the peaks are weak and not clearly observable in all spectra.

Figures 4.4 and 4.5 shows the trend for the Raman intensity of the 1185 cm^{-1} peak due to fluorescein and the 736 cm^{-1} due to the adenine moieties in the scaffold molecules. As expected, the intensity of the fluorescein peaks decays, as the fluorescein is placed further and further away from the nanoshell surface. On the other hand, the Raman intensity of the adenine peak increases with increasing tether length due to the larger number of adenine in each strand for longer lengths.

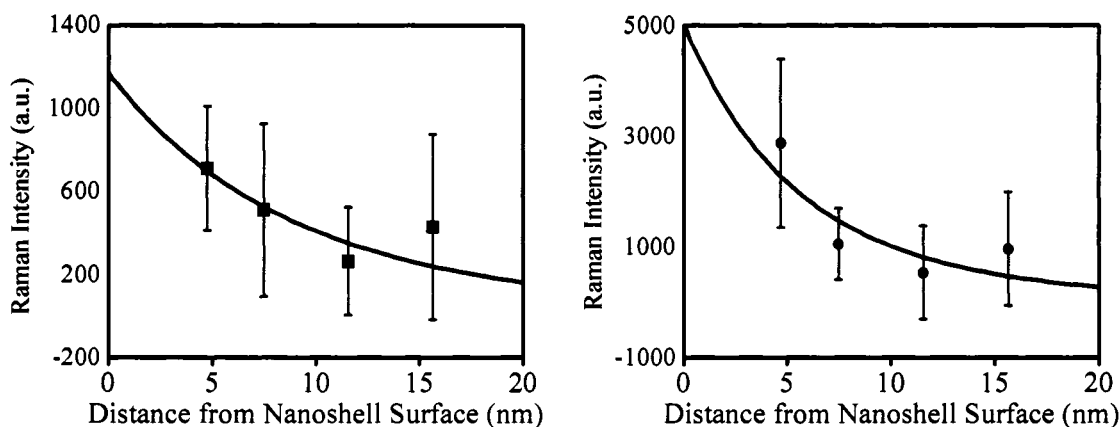


Figure 4.4: Intensity of the 1185cm^{-1} peak due to fluorescein (left) for $[r_1, r_2] = [70, 91]$ nm shells (squares) and (right) for $[r_1, r_2] = [43, 58]$ nm nanoshells (circles).

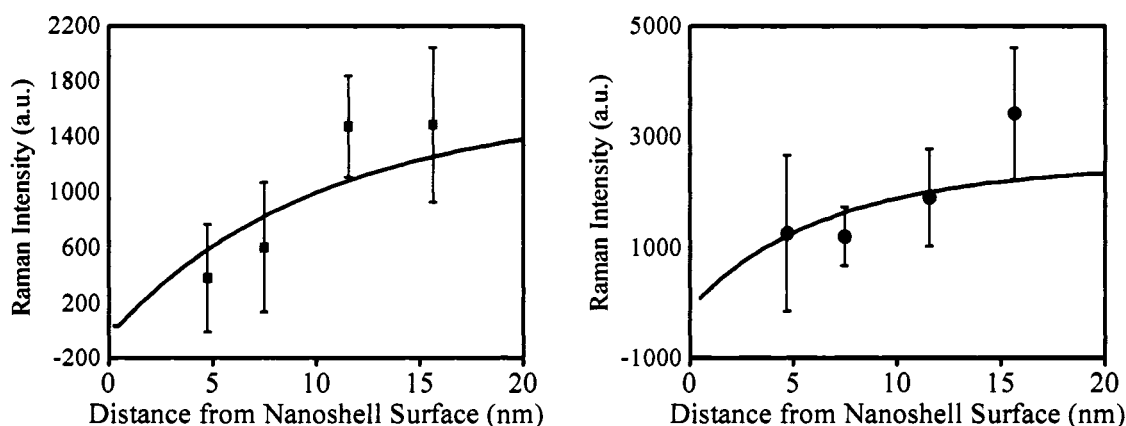


Figure 4.5: Intensity of the 736 cm^{-1} peak due to adenine (left) $[r_1, r_2] = [70, 91]$ nm shells (squares) and (right) for $[r_1, r_2] = [43, 58]$ nm nanoshells (circles).

Variations in the measured intensity are also likely due to the different packing densities of the differing DNA scaffold molecules on the nanoshells^{46, 57}. The shortest length of DNA tends to have the highest packing density under similar conditions of oligonucleotide solution concentration, buffer strength etc. To normalize for the differences in the packing density, the relative intensity of the fluorescein peak to the

adenine peak is calculated. As there is exactly one fluorescein molecule per DNA strand, this ratio denotes the intensity of the fluorescein molecule for a given number of adenine molecules. Figure 4.6 shows the calculated relative intensity of fluorescein with respect to the adenine peak and the theoretically calculated SERS response for the normalized fluorescein intensity. The theoretical fits are calculated using Mie scattering theory.

$$\langle E_{SERS} \rangle = \left\langle |E_{incident}(\lambda_L) + E_{NS}(\lambda_L)|^2 \cdot |E_{NS}(\lambda_S)|^2 \right\rangle \quad (4.1)$$

where $\langle E_{SERS} \rangle$ is the total surface averaged SERS response at the Raman emission wavelength. This is calculated as a product of the field intensity ($|E|^2$) at the laser excitation wavelength λ_L due to the incident laser ($E_{incident}$) and the nanoshell response (E_{NS}) at that wavelength, and the intensity at the Raman emission wavelength λ_S due purely to the nanoshell response at the shifted wavelength.

For both sets of nanoshells the experimental data follows the theoretically predicted SERS response trends.

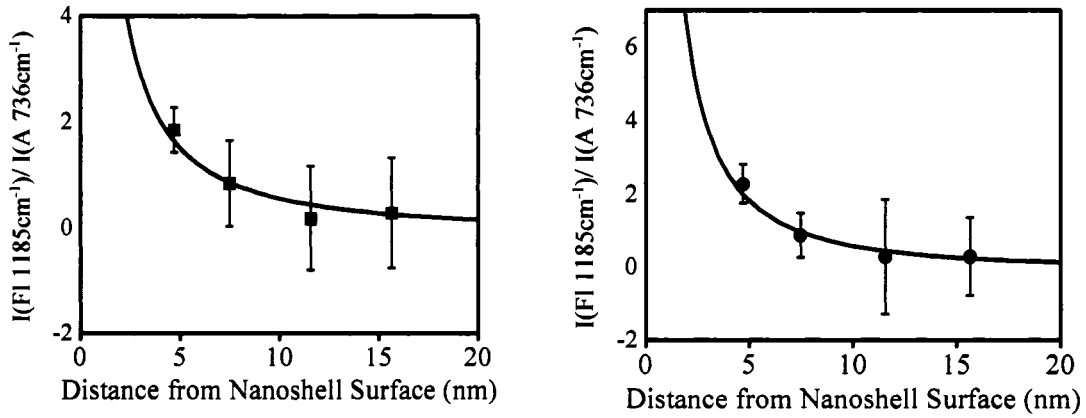


Figure 4.6 : Relative intensity of Fluorescein to adenine (left) for $[r_1, r_2] = [70, 91]$ nm shells and (right) for $[r_1, r_2] = [43, 58]$ nm nanoshells.

Figure 4.7 shows the theoretically calculated SERS enhancement factor for both sets of nanoshell substrates. Figure 4.7 (y axis) shows that the enhancement is almost two times as large for the smaller nanoshells with the near field maximum tuned to the pump laser. In spite of the larger enhancement and thus expected larger SERS signal, the overall signal intensity is smaller for the smaller nanoshells. This can be explained by considering the surface area of the nanoshells available for packing DNA strands. The larger nanoshells have a much larger surface area where the Raman active molecules can pack and thus gives a much larger signal. The smaller nanoshells have a larger enhancement factor but provide a much smaller surface area for Raman active molecules to attach to the surface. Thus in trying to design a nanoshell to get the largest SERS signal, along with the enhancement, the overall size of the nanoshells also needs to be considered.

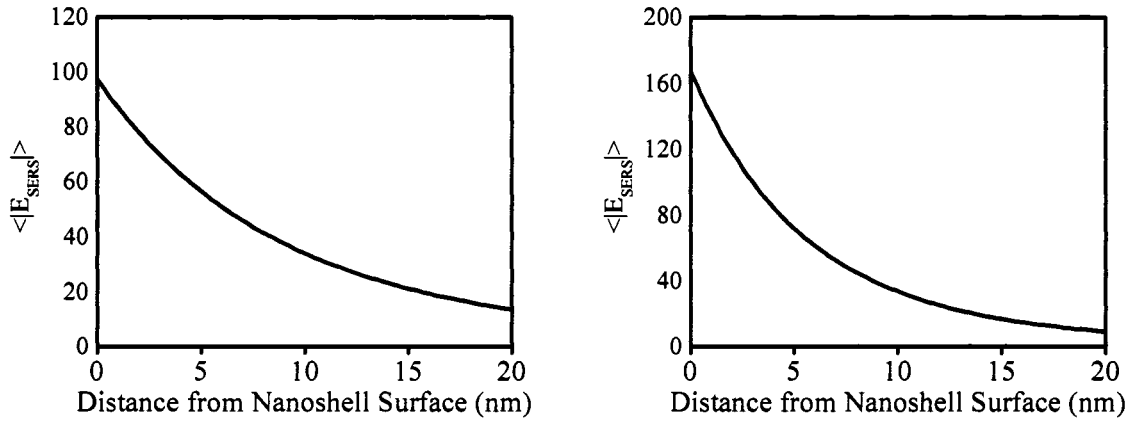


Figure 4.7: SERS enhancement factors calculated (left) for $[r_1, r_2] = [70, 91]$ nm shells and (right) for $[r_1, r_2] = [43, 58]$ nm nanoshells using equation 4.1.

4.3 Fluorescence Results

Fluorescence measurements were performed to determine i) the packing density of the ss-DNA on the nanoshells and ii) the change in the fluorescence intensity of the fluorescein molecule due to the increasing distance between the nanoshell surface and the fluorescein molecule. Measurements were performed for 4 different lengths of ss-DNA with 6, 12, 24, and 36 mixed bases.

To determine the packing density of the different lengths of DNA on the nanoshells, the various ss-DNA molecules were allowed to self assemble on the surface of the nanoshells in an aqueous buffer. Excess ss-DNA was removed from the solution by centrifugation and the final sample was redispersed in a 20 μ M solution of mercaptoethanol. The mercaptoethanol displaces the ss-DNA thiol bond on the gold surface releasing the ss-DNA into the solution. Next the nanoshells are removed from the solution by centrifuging the samples. The nanoshells are compacted into a small pellet at the bottom of the centrifuge tube. The concentration of the ss-DNA in the supernatant layer is then quantified against a series of standard solutions prepared from a known concentration of the same ss-DNA solution.

Figure 4.8 shows the packing density of the various lengths of DNA conjugated to the nanoshells. As can be seen in the figure, the shortest length consisting of 6 bases has a significantly higher concentration on the nanoshell surface. For the longer strands the concentration is much smaller. This trend is consistent with observations by other researchers studying attachment of ss-DNA to gold colloid^{46, 57}

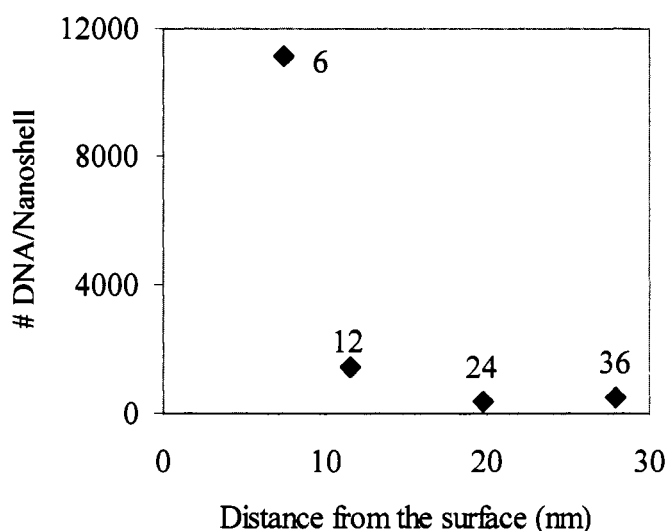


Figure 4.8 : Packing densities of the different lengths of ss-DNA. The number of bases in each length is denoted next to the data point.

In Figure 4.9 the variation in the fluorescence emission intensity at 516 nm per fluorescein molecule attached to nanoshells can be seen. Each data point is an average of at least 10 samples and has been normalized for the concentration of nanoshells in each sample, the attachment efficiency of the fluorescein conjugation to the oligonucleotide strands, and the packing density of different lengths of ss-DNA to the nanoshells. Although the attachment of fluorescein to the ss-DNA is efficient, it is not 100%. Small variations in fluorophore attachment occur from batch to batch of the same sequence with the same modifications (eg. the thiol modification of the 5' end of the ss-DNA in the present experiments). Thus the concentration of the DNA and of fluorescein are determined by measuring the absorbance of the DNA strand at 260 nm and fluorescein at 495 nm. The ratio of the concentration of fluorescein to the concentration of the DNA strand provides a measure of the attachment efficiency.

For the shortest DNA strand (6 bases) the fluorescein molecule is closest to the metal surface and hence its emission intensity is significantly quenched. From Figure 4.9 the variation in the per molecule fluorescence intensity is observed as the DNA strand length increases.

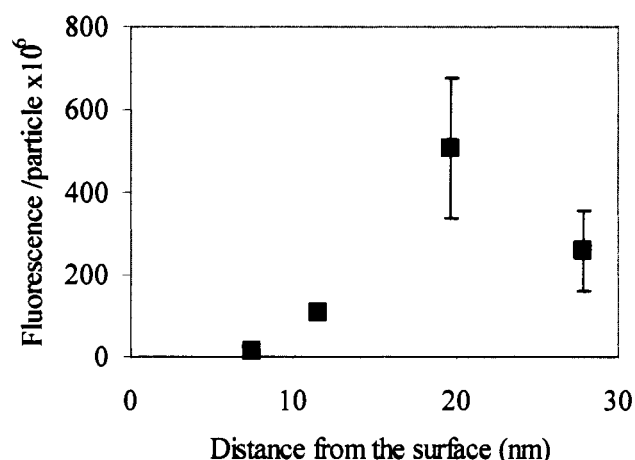


Figure 4.9 : Fluorescence per fluorescein molecule attached to nanoshells at different distances from the nanoshell surface.

For the longest length of ss-DNA, (36 bases) the ss-DNA may no longer be in a radially stretched configuration. It may have part of the strand in a stretched configuration, and part in a coiled floppy configuration. Parak et al.⁴⁵ have observed a similar configuration in longer (> 30 bases) ss-DNA strands attached to gold colloid. This leads to the reduction in intensity and a larger variation in intensity from one sample to the next, giving rise to the larger error bars. The longest strand may also be in a region where the near field enhancement is beginning to fall off significantly thus reducing the fluorescence emission intensity.

To quantify the effect of the nanoshell metal surface, the fluorescence enhancement is calculated. The enhancement is defined as the ratio of the fluorescence intensity when the ss-DNA-fluorescein strand is attached to the nanoshell to the intensity of the ss-DNA fluorescein strand in solution.

$$\text{Enhancement} = \frac{I_{Fl}^{NS}}{I_{Fl}} \quad (4.2)$$

Figure 4.10 a) shows the enhancement for the different lengths of DNA strands. For the shortest strand of 6 bases, the fluorescein molecule is ~ 7 nm from the surface and the intensity is reduced. Thus for distances of ~ 7 nm from the surface quenching due to the metal surface is the dominant process. For longer lengths of the DNA strand (12-36 bases) a small enhancement is observed.

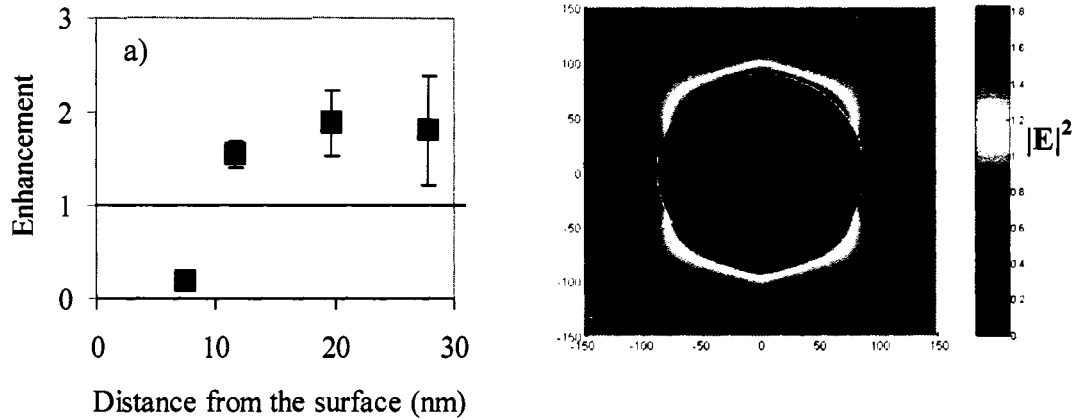


Figure 4.10: Enhancement in fluorescence intensity of fluorescein at different distances from the nanoshell surface b) Near field intensity distribution at 494 nm.

Although the nanoshells were designed to have a minimum absorption in the part of the spectrum where fluorescein absorbs, the nanoshell absorption is still nonzero in this regime. Figure 4.10 b) is a plot of the near field around the nanoshell at 494 nm (the absorption maximum of fluorescein) is consistent with the average enhancement of the near field.

4.4 *Fluorescein, Nanoshells and pH*

Fluorescein is a widely used fluorophore in biosciences. Its large quantum yield, well-developed conjugation chemistry, and low cost make it an attractive fluorophore for many applications. At the same time, the fluorescence emission of fluorescein is highly pH sensitive. As can be seen in figure 4.11, both the absorption and emission of fluorescein varies widely as the pH changes from 5-8. The fluorescence quantum yield decreases from 0.93 at pH 9 to 0.37 for pH 5.4. Thus maintaining the pH over 8 is crucial for the fluorescence measurements.

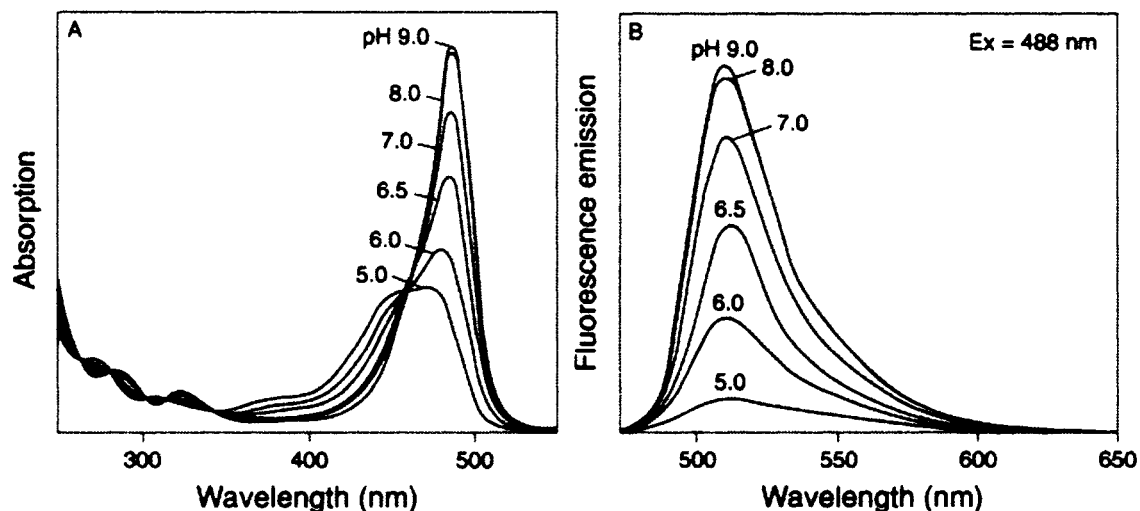


Figure 4.11 : pH dependence of the absorption and emission of fluorescein ⁵⁸.

Wang et al.⁵⁵ have reported the pH dependent Raman spectra of fluorescein. The intensity of the Raman mode at 1185cm^{-1} that has been analyzed for the SERS experiments has been shown to be pH sensitive and thus maintaining a $\text{pH} > 8$ is important for the SERS measurements.

As prepared nanoshells are stable in water but aggregate in most buffer solutions. The nanoshell surface needs to be protected before the nanoshells can be dispersed in most buffer solutions. For the SERS measurements, the nanoshells were immobilized on fused quartz substrates using poly-(4-vinyl)-pyridine (PVP). The ss-DNA nanoshell conjugates can then be immersed in buffer solutions for the SERS measurements. Nanoshells immobilized on glass slides using 3-aminopropyltriethoxysilane (APTES) are mobile and tend to aggregate on the surface when buffer solutions are added.

The nanoshells in samples prepared for the fluorescence measurements are dispersed in aqueous solution. After the formation of the mixed ss-DNA MCH monolayer on the nanoshells, the nanoshells were dispersed in a 10mM sodium phosphate buffer pH 8.3. The final step in the fluorescence sample preparation involved displacement of the ss-DNA from the nanoshells via a thiol displacement reaction using mercaptoethanol. Mercaptoethanol is highly acidic. Making dilutions of mercaptoethanol while maintaining a high pH proved to be a challenge. The final pH was adjusted using potassium carbonate as nanoshells are known to be stable in potassium carbonate solution. Although this approach is not optimal, the pH of the solutions could be maintained in a high pH regime.

4.5 Conclusion

The theoretically predicted distance dependence of near field profile has been experimentally verified using a DNA scaffold to attach and place fluorescein molecules at known distances around the nanoshells. The experimentally measured variation in the surface enhanced Raman intensity of fluorescein with distance have been shown to correlate well with theory for nanoshells whose plasmon or near field maximum is both resonant and non resonant with the excitation laser. The distance dependent fluorescence emission of fluorescein attached to nanoshells is also in good qualitative agreement with theoretically predicted trends. However to match the experimental results to a complete theoretical model would require further investigations.

Chapter 5 : Light Interaction between Nanoshell Plasmons and Planar Waveguides

5.1 Introduction

Noble metal nanoparticles are known for their ability to support resonant plasmon oscillations. When these nanoparticles are placed on a waveguiding structure that can support optical guided modes within the spectral range of the nanoparticle resonance, there is a coupling of the scattered light from the nanoparticles to the waveguide modes. Stuart and Hall⁵⁹ have shown qualitative changes in the scattering spectra of silver nanoparticles randomly placed over a waveguiding structure. Linden *et al.*⁶⁰ have studied the change in the extinction spectra of an array of gold nanoparticles deposited over a waveguiding structure. Both groups have attributed the observed changes to light coupling to the modes supported by the underlying structure.

In this section the interaction of gold nanoshells deposited on a waveguiding structure is discussed. The waveguiding structure consists of a 2 μ m gold film with a dielectric layer of different thickness deposited on it. Light scattering experiments performed on randomly deposited nanoshells, show a change in the scattering spectrum of nanoshells due to coupling with the optical waveguide modes. Comparison of the experimental spectra for different dielectric layer thickness with theoretical calculations based on the classic theory of point dipoles over a conducting surface shows significant shifts in the dipole resonance position. A simple image charge calculation taking into consideration the finite size of nanoshells accounts for most of the observed shifts⁶¹⁻⁶³.

5.2 Experimental Techniques

The nanoshells used in the following experiments consist of a silica core covered by a gold shell. The dipole resonance of the gold nanoshells was designed to be at 650 nm. The nanoshells used in the present experiment have a core radius $r_1 = 31$ nm and total

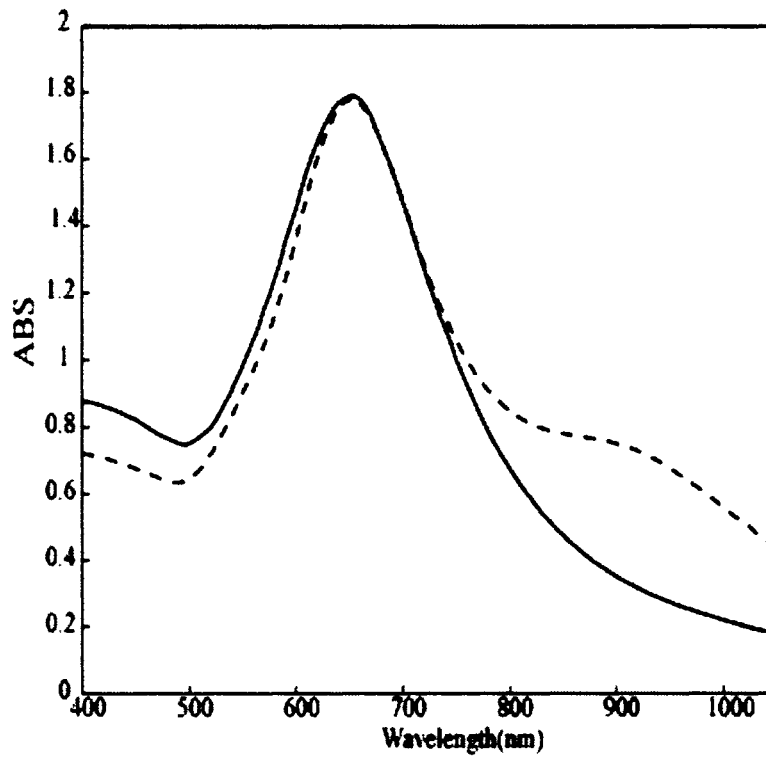


Figure 5.1 : UV-Visible spectrum (dashed line) and the calculated cross section (solid line) for an aqueous solution of gold nanoshells

particle radius $r_2 = 43$ nm. The average radius of the core is determined using transmission electron microscopy (TEM) and a statistical analysis of the TEM images.

The total particle radius is determined by a theoretical curve fitting to the UV-Visible spectrum of the nanoshells. The UV-Visible spectrum of an aqueous solution of nanoshells is shown in Figure 5.1

In addition to the strong dipole resonance peak at 650 nm, a second broader peak at 900 nm is seen due to the presence of doublets and other low order aggregates present in the solution³¹. The theoretical cross section was calculated using Mie scattering theory³⁰.

Figure 5.2 (a) shows a schematic of the sample geometry. An approximately 200 nm thick layer of gold was sputter coated onto an indium tin oxide (ITO) coated glass slide. Self-Assembled Monolayers (SAM's) of a cationic polyelectrolyte PDPA (poly(diallyldimethylammonium chloride) and anionic sheets of an exfoliated synthetic clay (Laponite RD, a synthetic form of hectorite)⁶⁴ were deposited on the gold surface to control the spacing s to nominally nm precision between the gold surface and the gold nanoshells. A sub monolayer of gold nanoshells (Figure 5. 2(b)), with an average spacing of 200 nm and approximately 27% coverage (as determined by scanning electron microscopy) was deposited on the SAM's by evaporating 10-20 μ l of concentrated aqueous solution containing nanoshells. Figure 5.2(b) also shows the presence of doublets and low order aggregates. Figure 5.2(c) is a digital camera photograph of scattered light from the samples. The left most image is the gold film without the dielectric layer. The thickness s of the dielectric spacer layer is given below each image.

For light scattering experiments the samples were illuminated at normal incidence by light from a tungsten-halogen lamp passed through a monochromator. The scattered light was collected over a wide angular range using a lens and a Hamamatsu S1336-

44BQ photodiode detector. All experimental data are shown to scale as acquired and have been reproduced on similar samples with similar nanoshell coverage to ensure consistency.

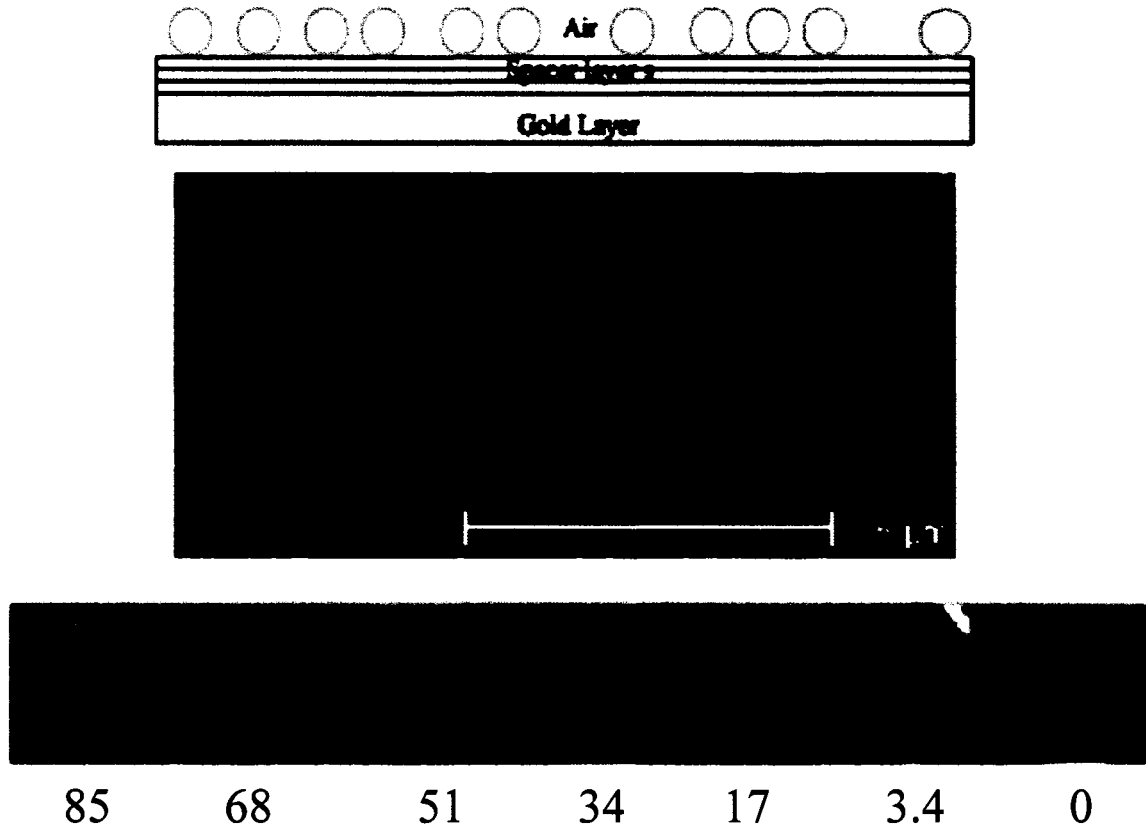


Figure 5.2 : (a) Schematic diagram of sample geometry. (b) SEM micrograph showing a typical distribution of nanoshells on the dielectric surface.(c) Digital camera photograph of scattered light from samples of thickness varying from 3.4 nm to 85 nm.

5.3 Results and Discussion

Figure 5.3 shows the modification in the nanoshell scattering spectrum due to interaction of the nanoshell resonance with the surface plasmon (SP) of the nearby gold surface. We can divide the surface plasmon-nanoshell plasmon interaction into three regimes depending upon the separation s . Spectra 5.3(a) and 5.3(b) for the smallest

separations, there is a significant overlap of the near field of the nanoshell with the surface plasmon mode. Here we observe the strong dipole peak that has shifted from 650 nm in water to 760 nm for $s = 3.4$ nm and to 694 nm for $s = 17$ nm. There is also an enhancement of the quadrupole peak at approximately 580 nm. As the thickness of the spacer layer increases (spectra 5.3(c) and 5.3(d)), we observe less enhancement of the dipole and quadrupole peaks, but the peak at 900 nm due to interparticle effects dominates. This enhancement of the peak due to interparticle interactions suggests that the surface plasmon mode mediate the interaction between nanoshells over a much longer distance, governed by the surface plasmon attenuation length. In the last two spectra for large separations, as the overlap between the nanoshell near field and the surface plasmon mode decreases, the broad peak due to the dipole and interparticle effects decreases and red shifts to longer wavelengths.

Theoretically, the energy transfer process can be explained using arguments similar to those used by Stuart and Hall⁵⁹ to explain the change in the scattering spectra of silver island films deposited on a silicon on insulator (SOI) structure. These arguments are based on the classic theory of a point dipole over a metal surface proposed by Chance Prock and Silbey (CPS)⁶⁵ and further developed by Weber and Ford⁶⁶ and Sullivan and Hall^{67, 68}. The CPS theory provides an energy transfer mechanism between an excited point dipole and the surface plasmon (and other propagating modes) that falls within the near field of the dipole. Stuart and Hall⁵⁹ carry the arguments further by considering an energy transfer path mediated by the propagating waveguide modes.

The incident white light is scattered by the nanoshells and couples to the surface plasmon mode. This interaction is thus proportional to $\sigma_s f_m$, where σ_s is the scattering cross section of the nanoshells and f_m is the fraction of scattered energy that couples to

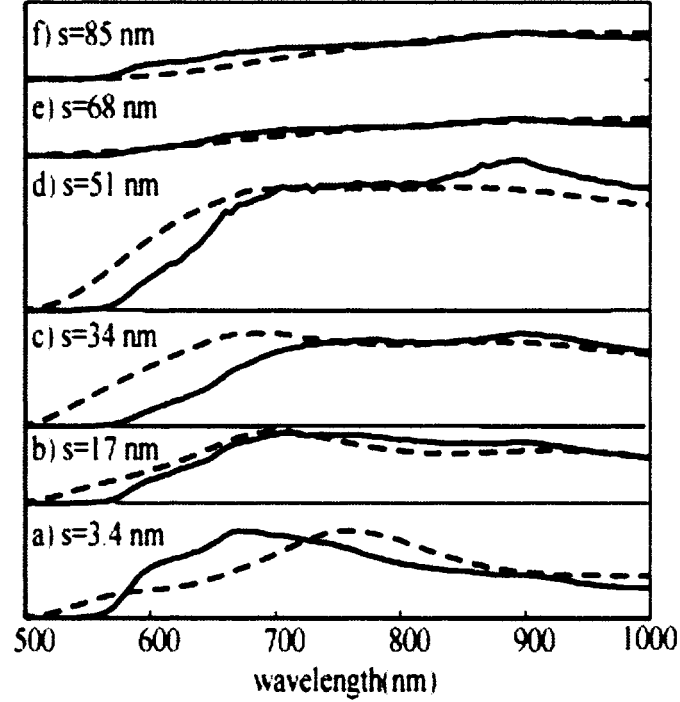


Figure 5.3: Light scattering spectra for various thickness of spacer layer. The dashed lines are the experimental data and the solid lines are the calculated theoretical spectra.

the SP mode. Due to reciprocity of light, the energy in the SP can couple out to the nanoshells via the same mechanism and thus is proportional to the same term $\sigma_s f_m$. The guided mode has a propagation length of L_m , and thus all the nanoshells within an area

proportional to L_m^2 can act as channels for the energy transfer from the SP to the nanoshells. Finally a fraction of this energy is scattered into air as f_{air} . Thus we can write the wavelength dependence of the total interaction as

$$\eta_m(\lambda) = (\sigma_s(\lambda) f_m(\lambda))^2 L_m^2(\lambda) f_{air}(\lambda) \quad (5.1)$$

The energy transfer interaction of equation (5.1) is shown in schematic form in figure 5.4.

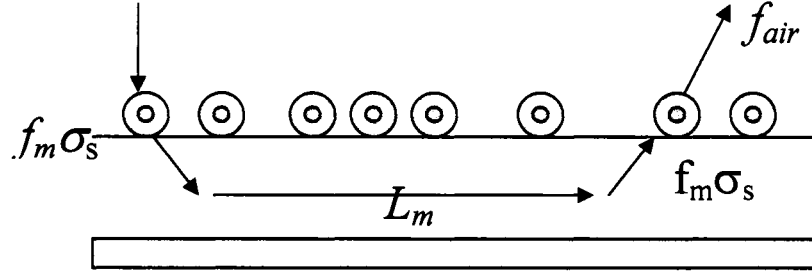


Figure .5.4: Schematic cartoon of the entire energy transfer interaction between the nanoshells and the waveguide structure.

Theoretical fits are done by using Eqn (5.1). To calculate $L_m(\lambda)$, the form of the electric fields for guided modes in each layer are written down and then continuity equations applied. This results in a transcendental equation for the propagation constant of the m^{th} mode, which can be numerically solved. Since the propagation constant is directly related to the effective indices of the mode, n_{eff} , the attenuation length is obtained by noting that $L_m(\lambda) = \lambda / (4\pi \text{Im}(n_{eff}))$. The energy coupling fractions, $f_m(\lambda)$ and $f_{air}(\lambda)$, are determined numerically from the equations for modified damping rates of dipoles near interfaces^{66, 69}. Figure 4 shows the comparison of the theoretical and experimental spectra for dielectric layer thickness from 3.4 nm to 85 nm.

On comparison we observe that for the smallest dielectric layer (spectrum 5.3(a)), the observed dipole peak is red shifted by about 65 nm with respect to the theoretically predicted peak. The quadrupole peak observed at 580 nm is not well fit by this theory, as

it assumes that a pure point dipole, and no higher order multipoles participate in the energy transfer process. As the dielectric spacer layer thickness increases (Figure 5.3(b), 5.3(c) and 5.3(d)), we observe a blue shift in the position of the dipole resonance peak, which shifts to wavelengths smaller than those predicted by theory. By shifting the theoretical curves, one can achieve a reasonable agreement with the experimental data. In figure 5.5 we show a comparison of the experimental data with the shifted theoretical curves. These shifts are listed in Table 1. A number of theoretical investigations of point dipoles interacting with conducting surfaces have shown surface induced shifts in the dipole resonance frequency⁷⁰⁻⁷³.

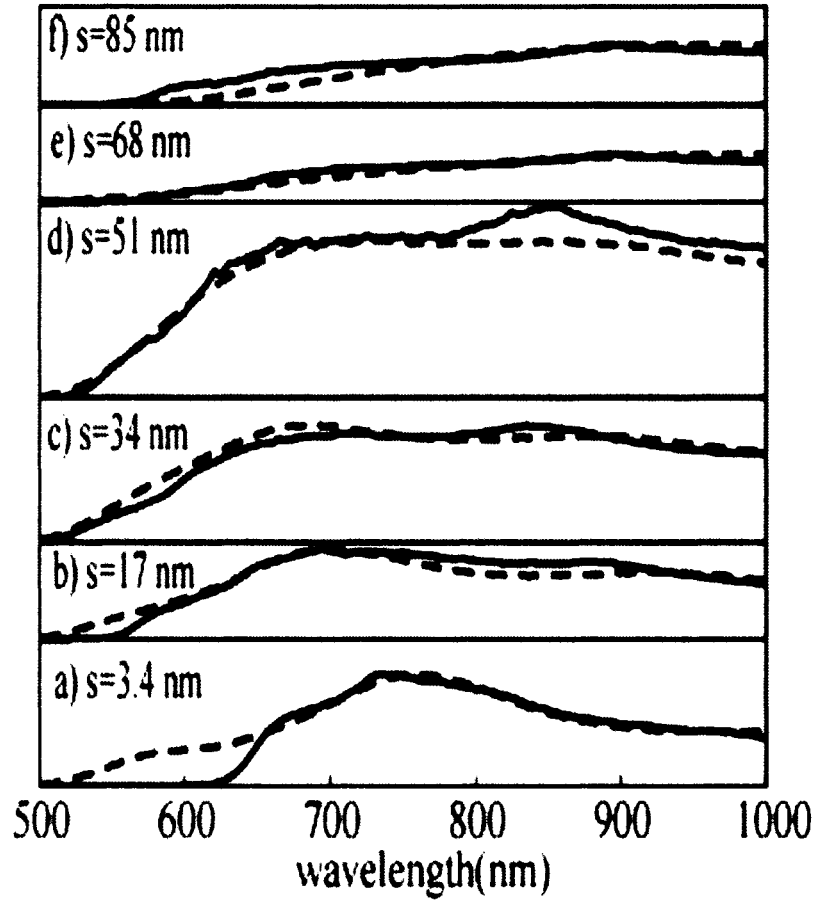


Figure 5.5: Comparison of the experimental light scattering spectra and the shifted theoretical curves. The dashed lines are the experimental data and the solid lines are the calculated theoretical spectra, shifted by amount shown in Table 5.1.

Table 5.1: Experimental and theoretical shift in dipole peak position for different spacer layer thickness.

Spacer Layer Thickness	Shift in peak position	CPS Theory	Image charge Theory
3.4 nm	+ 65 nm	+2.4 nm	+26 nm
17 nm	- 15 nm	-25 nm	+11 nm
34 nm	- 60 nm	-32.7 nm	+4.9 nm
51 nm	- 40 nm	- 26 nm	+2.6 nm
68 nm	0	- 18 nm	+1.6 nm
85 nm	0	-14.2 nm	+1.0 nm

The basic trends of these shifts can be understood by considering the reflected field (E_{ref}) incident at the position of the dipole. For purposes of this analysis, the nanoshell is approximated by a point dipole. Chance, Prock and Silbey⁷¹ derived an approximate expression for the frequency shift of the dipole resonance, $\Delta\omega$ due to E_{ref} .

$$\frac{\Delta\omega}{b_\infty} \approx -\frac{3}{4} \gamma \operatorname{Re} \left(\frac{\epsilon_l E_{ref}}{k^3 \mu_0} \right) \quad (5.2)$$

Here, b_∞ is the decay rate (the lifetime of the resonance) in the absence of an interface, ϵ_l is the dielectric constant of the medium in which the dipole (the nanoshell) is embedded, k_l is the wave-vector in that region, γ is the quantum yield of the emitting state and μ_0 is the dipole moment. For the current discussion γ is taken to be 1. Both the magnitude and

the sign of the frequency shift depend critically on the reflected field at the position of the dipole. Therefore, it is important to know how E_{ref} behaves with change in dielectric layer thickness. The use of appropriate Fresnel coefficients at both interfaces gives the net reflected field at the dipole position. E_{ref} changes sign as the spacer layer thickness changes. This is true for both the parallel and perpendicular polarization of light. For normal incidence of light, E_{ref} goes from a positive to a negative value with increasing value of s , suggesting a transition from red to blue shifts in the dipole resonance position. Similar results are obtained for the case of parallel polarization. The shifts calculated using Equation 5.2 for the spacer layer thickness in the experiment are listed in Table 5.1. These shifts are in qualitative agreement with shifts used in Figure 5.6.

The large red shift observed for the thinnest dielectric films cannot be explained using CPS theory. The CPS theory treats the dipoles as point dipoles. A physical effect absent from the CPS theory is the effect of the image interaction of a finite dipole with a conducting surface.

A simple approach to modeling the plasmon oscillations of the conduction electrons of the nanoshell as a rigid translation of spherical charge distribution with respect to its positive background has been developed. A simple horizontal dipole of finite size is depicted in Figure 5.7. The image interaction between the finite dipole and the conducting surface results in a red shift of the dipole plasmon frequency. For horizontal polarization the image charge model predicts

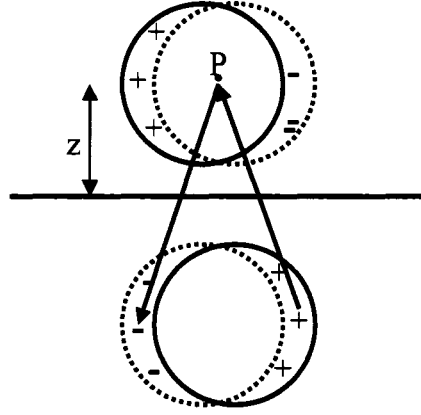


Figure 5.6: Schematic diagram of a horizontal image plasmon induced in the gold film.

$$\Delta\omega_p^H(z, R) = \omega_p^0 \left\{ 1 - \sqrt{1 - \left[9 \left(\frac{z}{R} \right)^2 + 1 \right]^{-\frac{3}{2}}} \right\} \quad (5.3)$$

and for vertical polarization the shift in frequency is

$$\Delta\omega_p^V(z, R) = \omega_p^0 \left\{ 1 - \sqrt{1 - 6 \frac{z}{R} \left[9 \left(\frac{z}{R} \right)^2 - 1 \right]^{-2}} \right\} \quad (5.4)$$

where $\Delta\omega_p$ is the theoretical dipole resonance frequency shift from the experimentally observed resonance frequency ω_p^0 , z is the distance of the center of the spherical particle from the conducting surface and R is its radius. The calculated shifts for the vertical polarization are included in Table 5.1. As can be seen, the model predicts a relatively strong red shift for the thinnest dielectric layer, and subsequently smaller red shifts for larger spacer layer thickness.

5.4 Conclusion

In conclusion the light scattering spectrum of the nanoshells is modified due to the presence of an underlying waveguiding structure. We have measured the shifts in the

scattering spectra as a function of the gold nanoshell-gold surface separation. The nanoshell- surface plasmon interaction is strongly dependent on overlap of the gold nanoshell near field and the surface plasmon mode and thus on the gold nanoshell-gold surface separation. The classical CPS theory does not take into consideration the finite size of the nanoshell and thus fails to explain the large red shifts observed for the smallest spacer layer thickness. We have developed a simple model considering the nanoshell as a finite sized dipole and the forces exerted on it due to the presence of its image charge. The image charge theory shows similar trends to those observed and gives much better agreement with the large red shift for the smallest separations.

This set of measurements and the accompanying theoretical model to explain the observed shifts and interaction peak was developed before the more intuitive plasmon hybridization theory. Plasmon hybridization theory can be used to explain the interaction between the nanoshell plasmon and the surface plasmon of the smooth gold film. This system of a nanoshell over a thick smooth gold film is complex. A similar simpler system of a solid gold nanoparticles on a thin gold smooth film has been recently investigated⁷⁴. This is a first step in understanding the more complex problem of the distance dependent interaction of a nanoshell plasmon with a thick gold film plasmon. In future this experiment can be repeated with better control over film thickness by evaporating the gold film rather than sputter coating the gold film. Nanoshell solutions of small nanoshell with resonances in the visible part of the spectrum can be synthesized with fewer aggregates. This would clarify the plasmon- plasmon interaction spectrum. Computational methods using finite difference time domain (FDTD) have successfully implemented plasmon hybridization theory to model the solid nanosphere plasmon

interaction with smooth gold film plasmon ⁷⁴. These methods have also been successfully applied in investigating plasmon plasmon interactions in nanoshells and concentric nanoshells ^{32, 35} Thus in future FDTD implementation of the plasmon hybridization can be further expanded to study more complex systems like the present one.

Chapter 6 : Conclusions

In this thesis a systematic experimental mapping of the enhanced near field of silica gold nanoshells is investigated using surface enhanced Raman spectroscopy (SERS) and metal enhanced Fluorescence spectroscopy (MEFS). Silica gold nanoshells are studied as they have well-controlled and reproducible geometry. The electromagnetic problem of light interaction with a nanoshell is well understood. There are well-established analytical solutions to the electromagnetic interaction of nanoshells with light. This forms the basis for the theoretical prediction of the near field profile of the nanoshells.

To experimentally map out the near field profile, the SERS response of the Raman active fluorescein dye molecules placed at well-controlled distances from the nanoshell surface is measured. ss-DNA are used to form the tether linking the fluorescein molecules to the nanoshell surface. The length of the tether is varied systematically to measure the Raman response at different distances from the surface. The SERS response to two different sets of nanoshells is measured. The first set of nanoshells is designed with the far field dipole response tuned to the excitation laser. The second set of nanoshells is designed with the near field dipole response tuned to the excitation laser. The measured SERS response for the various tether lengths is correlated to the theoretically predicted SERS response for both sets of nanoshells and is found to be in very good agreement. The correlation is excellent considering the fact that the ss-DNA does not form a rigid tether but is highly flexible. The enhanced Raman signals were

measured for length scales from ~ 4 nm to 15 nm. The normalized enhanced signal persists for lengths > 15 nm.

Although the theoretically predicted near field intensity and hence the Raman response of the nanoshells with the near field dipole peak tuned to the excitation laser is much larger than the predicted near field enhancement of the nanoshells with the extinction tuned to the excitation laser, the overall measured SERS signal was smaller. This was found to be due to the much smaller size of the nanoshells with the near field dipole tuned to the laser. The smaller size provides a much smaller surface area for the fluorescein to attach to and thus the total number of Raman active dye molecules is much smaller. This is an important design consideration for sensor devices using SERS. An optimal size of nanoshells with large enhancements at the excitation laser is needed to get the largest Raman response.

For sensor devices using fluorescence intensity, the distance at which a fluorophore can be placed in front of a metal surface is an important design parameter. Very close to the nanoshell surface where the near field enhancement is maximum, the metal surface quenches the fluorescence intensity by providing a non-radiative decay pathway for the fluorophore to relax. Thus there is an optimal distance in front of the metal surface where the quenching is not the dominant process and the enhanced near field can be used to enhance the fluorescence signal. The second series of experiments explores the quenching regime between ~ 4 nm and ~ 30 nm. Fluorescence intensity of fluorescein attached to silica gold nanoshells via ss-DNA of various lengths are measured. For the shortest distance ~ 5 nm there is quenching of the fluorescence signal. For all other distances a small enhancement consistent with the near field enhancement at

that wavelength is observed. For the largest distance from the surface ~ 30 nm a drop off in the fluorescence signal is observed. This can be due to a fall off in the enhanced field and due to the larger flexibility of the longer ss-DNA tether.

One of the hardest parameters to control in the fluorescence measurements was the pH of the solution. Nanoshells are unstable and aggregate in most buffer solutions. The nanoshell surface needs to be protected before the nanoshells can be dispersed in a buffer solution. Also, the thiol displacement reaction with mercaptoethanol results in a solution with an acidic pH. The fluorescence intensity of fluorescein is highly pH sensitive for pH below 8. Thus to maintain a pH over 8, and not have nanoshells aggregate over the time it takes to make the samples and measure the entire series of samples proved to be a significant challenge. In the future, the fluorescence measurements could be repeated easily with a different fluorophore attached to the ss-DNA whose fluorescence is not pH dependent. There are many suitable dye molecules, such as the Alexa dyes and Oregon Green that have absorption and emission peaks in the same part of the spectrum as fluorescein, can be easily conjugated to ss-DNA, and are not pH sensitive and do not photo bleach as easily as fluorescein. To use fluorescein as the fluorophore, buffers in which nanoshells are stable need to be investigated. There is some evidence that a 100mM borate buffer may offer the required pH and buffering capabilities.

The last set of experiments focuses on the distance dependence of the interaction of the nanoshell plasmon and plasmon on a gold surface. Light scattering from nanoshells as a function of the nanoshell gold film separation is modeled on the classical theory of a dipole in front of a mirror by Chance Prock and Silbey. The classical CPS theory is for a

point dipole and thus fails to explain the large red shifts observed for the smallest spacer layer thickness. We have developed a simple model for a finite dipole in front of a mirror and the forces exerted on it due to the presence of its image charge. The image charge theory shows similar trends to those observed for nanoshells in front of a mirror and gives much better agreement with the large red shift for the smallest separations.

The light scattering from nanoshells placed on the gold surface, measurements was performed before an understanding of the plasmon plasmon interactions based on the plasmon hybridization had been developed. In light of the intuitive understanding of the plasmon- plasmon interaction based on the plasmon hybridization theory, the interactions can be modeled as distance dependant interaction between a nanoshell plasmon and the surface plasmon of the gold film. This is still a fairly complex system. A simpler system consisting of a solid gold sphere placed over a thin gold film has been recently investigated ⁷⁴. Future investigations could build on this investigation to better model and understand the interactions between a gold nanoshell plasmon and the surface plasmon of a smooth gold film.

Bibliography

1. Moscovits, M. Surface-enhanced spectroscopy. *Reviews of Modern Physics* 57 (1985).
2. Kreibig, U. & Vollmer, M. *Optical Properties of Metal Clusters* (Springer, New York, 1995).
3. Grady, N. K., Halas, N. J. & Nordlander, P. Influence of dielectric function properties on the optical response of plasmon resonant metallic nanoparticles. *Chemical Physics Letters* 399, 167-171 (2004).
4. Kelly, K. L., Eduardo, C., Zhao, L. L. & Schatz, G. C. The Optical Properties of Metal Nanoparticles: The Influence of Size, Shape, and Dielectric Environment. *J. Phys. Chem. B* 107, 668-677 (2003).
5. Ekgasit, S., Thammacharoen, C., Yu, F. & Knoll, W. Evanescent field in surface plasmon resonance and surface plasmon field-enhanced fluorescence spectroscopies. *Analytical Chemistry* 76, 2210-2219 (2004).
6. Jackson, J. B. & Halas, N. J. Surface-enhanced Raman scattering on tunable plasmonic nanoparticle substrates. *Proc. Natl. Acad. Sci.* vol. 101, 17930-17935 (2004).
7. Szafranski, C. A., Tanner, W., Laibinis, P. E. & Garrell, R. L. Surface-Enhanced Raman Spectroscopy of Aromatic Thiols and Disulfides on Gold Electrodes. *Langmuir* 14, 3570 (1998).
8. Jackson, J. B., Westcott, S. L., Hirsch, L. R., West, J. L. & Halas, N. J. Controlling the surface enhanced Raman effect via the nanoshell geometry. *Applied Physics Letters* Volume 82 (2003).
9. Karen Faulds, Rachael E. Littleford, Duncan Graham, Geoffrey Dent & Smith, W. E. Comparison of Surface-Enhanced Resonance Raman Scattering from Unaggregated and Aggregated Nanoparticles. *Anal. Chem* 76, 592-598 (2004).

10. Kennedy, B. J., Spaeth, S., Dickey, M. & Carron, K. T. Determination of the Distance Dependence and Experimental Effects for Modified SERS Substrates Based on Self-Assembled Monolayers Formed Using Alkanethiols. *J. Phys. Chem. B* 103, 3640-3646 (1999).
11. Kneipp, K. et al. Single Molecule Detection Using Surface-Enhanced Raman Scattering (SERS). *Phys. Rev. Lett.* 78, 1667-1670 (1997).
12. Knobloch, H., Brunner, H., A. Leitner, F. Aussenegg & Knoll, W. Probing the evanescent field of propagating plasmon surface polaritons by fluorescence and Raman spectroscopies. *J. Chem. Phys.* 98, 10093-10095 (1993).
13. Moskovits, M., Tay, L. L., Yang, J. & Haslett, T. in *Optical Properties Of Nanostructured Random Media* 215-226 (2002).
14. Oldenburg, S. J., Westcott, S. L., Averitt, R. D. & Halas, N. J. Surface enhanced Raman scattering in the near infrared using metal nanoshell substrates. *J. Chem. Phys.* 111, 4729-4735 (1999).
15. Kneipp, K. et al. Single-Molecule Detection of a Cyanine Dye in Silver Colloidal Solution Using Near-Infrared Surface-Enhanced Raman Scattering. *Applied Spectroscopy* 52, 175 (1998).
16. Kneipp, K. et al. Detection and Identification of a Single DNA Base Molecule using Surface-Enhanced Raman Scattering (SERS). *Phys. Rev. E* 57, R6281 (1998).
17. Joanna Lukomska, Joanna Malicka, Ignacy Gryczynski & Lakowicz, J. R. Fluorescence Enhancements on Silver Colloid Coated Surfaces. *Journal of Fluorescence*, Vol. 14, 417-423 (2004).
18. Malicka, J., Gryczynski, I., Gryczynski, Z. & Lakowicz, J. R. Effects of fluorophore-to-silver distance on the emission of cyanine dye-labeled oligonucleotides. *Analytical Biochemistry* 315, 57-66 (2003).
19. Sokolov, K., Chumanov, G. & Cotton, T. M. Enhancement of molecular fluorescence near the surface of colloidal metal films. *Anal. Chem.* 70, 3898-3905 (1998).

20. Thomas, K. G. & Kamat, P. V. Making Gold Nanoparticles Glow: Enhanced Emission from a Surface-Bound Fluorophore. *J. Am. Chem. Soc.* 122, 2655-2656 (2000).
21. Lakowicz, J. R. *Principles of Fluorescence Spectroscopy* 2nd Edition (Kluwer Academic/Plenum Publishers, 1999).
22. Mie, G. Articles on the optical characteristics of turbid tubes, especially colloidal metal solutions. *Annalen Der Physik* 25, 377-445 (1908).
23. David D. Evanoff, J., White, R. L. & Chumanov, G. Measuring the Distance Dependence of the Local Electromagnetic Field from Silver Nanoparticles. *J. Phys. Chem. B* 108, 1522-1524 (2004).
24. Sonnichsen, C., Reinhard, B. M., Liphardt, J. & Alivisatos, A. P. A molecular ruler based on plasmon coupling of single gold and silver nanoparticles. *Nature Biotechnology* 23, 741-745 (2005).
25. Reinhard, B. M., Siu, M., Agarwal, H., Alivisatos, A. P. & Liphardt, J. Calibration of Dynamic Molecular Rulers Based on Plasmon Coupling between Gold Nanoparticles. *Nano Letters* 5, 2246-2252 (2005).
26. Dulkeith, E. et al. Gold Nanoparticles Quench Fluorescence by Phase Induced Radiative Rate Suppression. *Nano Letters* Vol. 5, 585-589 (2005).
27. Yun, C. S. et al. Nanometal Surface Energy Transfer in Optical Rulers, Breaking the FRET Barrier. *J. Am. Chem. Soc.* 127, 3115-3119 (2005).
28. Tovmachenko, O. G., Christina Graf, Heuvel, D. J. v. d., Blaaderen, A. v. & Gerritsen, H. C. Fluorescence Enhancement by Metal-Core/Silica-Shell Nanoparticles. *Adv. Mater.* 18, 91-95 (2006).
29. Jackson, J. B. & Halas, N. J. Silver Nanoshells: Variations in Morphologies and Optical Properties. *J. Phys. Chem. B* 105, 2743-2746 (2001).
30. Oldenburg, S. J., Averitt, R. D. & Westcott, S. L. Nanoengineering of optical resonances. *Chem. Phys. Lett.* 288, 243 (1998).

31. Oldenburg, S. J., Jackson, J. B., Westcott, S. L. & Halas, N. J. Infrared Extinction Properties of Gold Nanoshells. *Appl. Phys. Lett.* 75, 2897-2899 (1999).
32. Prodan, E. & Nordlander, P. Plasmon hybridization in spherical nanoparticles. *Journal of Chemical Physics* 120, 5444-5454 (2004).
33. Nordlander, P., Oubre, C., Prodan, E., Li, K. & Stockman, M. I. Plasmon hybridization in nanoparticle dimers. *Nano Letters* 4, 899-903 (2004).
34. Nordlander, P. & Prodan, E. Plasmon hybridization in nanoparticles near metallic surfaces. *Nano Letters* 4, 2209-2213 (2004).
35. Prodan, E., Radloff, C., Halas, N. J. & Nordlander, P. A Hybridization Model for the Plasmon Response of Complex Nanostructures. *SCIENCE* Vol. 302, 419-422 (2003).
36. Radloff, C. & Halas, N. J. Plasmonic properties of concentric nanoshells. *Nano Letters* 4, 1323-1327 (2004).
37. Aden, A. L. & Kerker, M. Scattering of Electromagnetic Waves from Two Concentric Spheres. *J. App. Phys.* 22, 1242 (1951).
38. Lakowicz, J. R. Radiative Decay Engineering: Biophysical and Biomedical Applications. *Analytical Biochemistry* 298, 1-24 (2001).
39. Sarkar, D. & Halas, N. J. General vector basis function solution of Maxwell's equations. *Phys. Rev. E* 56, 1102-1112 (1997).
40. Sarkar, D. in *Electrical and Computer Engineering* (William Marsh Rice University, Houston, 1997).
41. Wang, H. et al. Symmetry-breaking in individual plasmonic nanoparticles. Submitted for publication (2006).
42. Nehl, C. L. et al. Scattering Spectra of Single Gold Nanoshells. *Nano Letters* 4, 2355-2359 (2004).

43. Oldenburg, S. J. in *Applied Physics* (William Marsh Rice University, Houston TX, 1999).
44. Stober, W., Fink, A. & Bohn, E. Controlled Growth of Monodisperse Silica Spheres in the Micron Size Range. *Journal Of Colloid And Interface Science* 26, 62-69 (1968).
45. Parak, W. J. et al. Conformation of Oligonucleotides Attached to Gold Nanocrystals Probed by Gel Electrophoresis. *Nano Letters* Vol. 3, 33-36 (2003).
46. Rant, U. et al. Structural Properties of Oligonucleotide Monolayers on Gold Surfaces Probed by Fluorescence Investigations. *Langmuir* 20, 10086-10092 (2004).
47. Sheng, R., Ni, F. & Cotton, T. M. Determination of Purine Bases by Reversed-Phase High-Performance Liquid Chromatography Using Real-Time Surface-Enhanced Raman Spectroscopy. *Anal. Chem.* 63, 437-442 (1991).
48. Zhang, R.-Y. et al. Investigation of Ordered ds-DNA Monolayers on Gold Electrode. *J. Phys. Chem. B* 106, 11233-11239 (2002).
49. Suh, J. S. & Moskovits, M. Surface-Enhanced Raman Spectroscopy of Amino Acids and Nucleotide Bases Adsorbed on Silver. *J. Am. Chem. Soc.* 108, 4711-4718 (1986).
50. Demers, L. M. et al. A Fluorescence-Based Method for Determining the Surface Coverage and Hybridization Efficiency of Thiol-Capped Oligonucleotides Bound to Gold Thin Films and Nanoparticles. *Analytical Chemistry* 72, 5535-5541 (2000).
51. Montalti, M. et al. Kinetics of Place-Exchange Reactions of Thiols on Gold Nanoparticles. *Langmuir* 19, 5172-5174 (2003).
52. Malynych, S., Luzinov, I. & Chumanov, G. Poly(Vinyl Pyridine) as a Universal Surface Modifier for Immobilization of Nanoparticles. *J. Phys. Chem. B*, 106, 1280-1285 (2002).
53. Herne, T. M. & Tarlov, M. J. Characterization of DNA Probes Immobilized on Gold Surfaces. *J. Am. Chem. Soc.* 119, 8916-8920 (1997).

54. Park, S., Brown, K. A. & Hamad-Schifferli, K. Changes in Oligonucleotide Conformation on Nanoparticle Surfaces by Modification with Mercaptohexanol. *NANO LETTERS* 4, 1925-1929 (2004).
55. Wang, L., Roitberg, A., Meuse, C. & Gaigalas, A. K. Raman and FTIR spectroscopies of fluorescein in solutions. *Spectrochimica Acta Part A* 57, 1781-1791 (2001).
56. Levin, C. S. Private Communication.
57. Pen˜a, S. R. N., Raina, S., Glenn P. Goodrich, Fedoroff, N. V. & Keating, C. D. Hybridization and Enzymatic Extension of Au Nanoparticle-Bound Oligonucleotides. *J. AM. CHEM. SOC.* 124, 7314-7323 (2002).
58. Molecular Probes Handbook.
59. Stuart, H. R. & Hall, D. G. Enhanced Dipole-dipole Interaction between Elementary Radiators Near a Surface. *Phys. Rev. Lett.* 80, 5663-5666 (1998).
60. Linden, S., Kuhl, J. & Gissen, H. Controlling the Interaction between Light and Gold Nanoparticles: Selective Suppression of extinction. *Phys. Rev. Lett.* 86, 4688-4691 (2001).
61. Lal, S., Taylor, R. N., Westcott, S. L., Jackson, J. B. & Halas, N. J. Plasmon-Plasmon Interaction between gold nanoshells and gold surfaces. *Bulletin of the A. P. S.* 46, 476 (2001).
62. Lal, S. et al. Plasmon- Plasmon Interaction between gold nanoshells and gold surfaces. *Trends in optics and photonics QELS 2001 Technical Digest* 57, 49-50 (2001).
63. Lal, S. et al. Light interaction between gold nanoshells plasmon resonance and planar optical waveguides. *Journal of Physical Chemistry B* 106, 5609-5612 (2002).
64. Klienfeld, E. R. & Ferguson, G. S. Stepwise Formation of Multilayered Nanostructural Films from Macromolecular Precursors. *Science* 265, 370-373 (1994).

65. Chance, R. R., Prock, A. & Silbey, R. Molecular fluorescence and energy transfer near interfaces. *Adv. Chem. Phys.* 37, 1-65 (1978).
66. Ford, G. W. & Weber, W. H. Electromagnetic Interactions of Molecules with Metal Surfaces. *Phys. Rep.* 113, 195-287 (1984).
67. Sullivan, K. G. & Hall, D. G. Enhancement and Inhibition of electromagnetic radiation in Plane-layered media. II. Enhanced Floresence in optical waveguide sensors. *J. Opt. Soc. Am. B* 14, 1160-1166 (1997).
68. Sullivan, K. G. & Hall, D. G. Enhancement and Inhibition of electromagnetic radiation in Plane-layered media. I Plane-wave spectrum approach to modelling classical effects. *J. Opt. Soc. Am. B* 14, 1160-1167 (1997).
69. Chance, R. R., Prock, A. & Silbey, R. in *Advances in Chemical Physics* (eds. Prigigine, I. & Rice, S. A.) 1-65 (Wiley, New York, 1978).
70. Aravind, P. K. & Metiu, H. The effects of the interaction between resonances in the electromagnetic response of a sphere-plane structure; applications to surface enhanced spectroscopy. *Surf. Sci.* 124, 506 (1983).
71. Chance, R. R., Prock, A. & Silbey, R. Frequency shifts of an electric-dipole transition near a partially reflecting surface. *Phys. Rev. A* 12, 1448-1452 (1975).
72. Kuhn, H. Classical aspects of energy transfer in molecular systems. *J. Chem. Phys.* 53, 101-8 (1970).
73. Morawitz, H. Self-coupling of a two level system by a mirror. *Phys. Rev.* 187, 1792-6 (1969).
74. Le, F. et al. Plasmons in the Metallic Nanoparticle-Film System as a Tunable Impurity Problem. *Nano Letters* 5, 2009-2013 (2005).